




Nanoparticles of ZnO/Berberine complex contract COVID-19 and respiratory co-bacterial infection in addition to elimination of hydroxychloroquine toxicity

Doaa A. Ghareeb^{1,2,3} · Samar R. Saleh^{1,2,3} · Mohamed G. Seadawy⁴ · Mohammed S. Nofal¹ · Shaymaa A. Abdulmalek^{1,2,3} · Salma F. Hassan¹ · Shaimaa M. Khedr¹ · Miral G. AbdElwahab¹ · Ahmed A. Sobhy^{1,2,5} · Ali saber Ali Abdel-Hamid¹ · Abdelrahman Mohamed Yassin¹ · Alshimaa A. Abd Elmoneam^{2,3} · Aliaa A. Masoud^{2,3} · Mohamed M. Y. Kaddah¹ · Sally A. El-Zahaby⁶  · Abdulaziz Mohsen Al-mahallawi^{7,8} · Alaa M. El-Gharbawy¹ · Ahmed Zaki¹ · Inas k. Seif^{1,2,3} · Marwa Y. Kenawy^{2,3,9} · Magdy Amin¹⁰ · Khaled Amer¹¹ · Maha Adel El Demellawy^{1,12}

Received: 22 April 2021 / Accepted: 22 August 2021 / Published online: 6 September 2021
© The Korean Society of Pharmaceutical Sciences and Technology 2021

Abstract

Purpose A novel coronavirus (COVID-19) that has not been previously identified in humans and has no specific treatment has recently spread. Treatment trials using antiviral and immune-modulating drugs such as hydroxychloroquine (HCQ) were used to control this viral outbreak however several side effects have emerged. Berberine (BER) is an alkaloid that has been reported to reveal some pharmacological properties including antioxidant and antimicrobial activities. Additionally, Zinc oxide nanoparticles (ZnO-NPs) possess potent antioxidant and anti-inflammatory properties. Therefore, this study was undertaken to estimate the efficiency of both BER and synthetic ZnO/BER complex as an anti-COVID-19 therapy.

Methods First, the ZnO/BER complex was prepared by the facile mixing method. Then *in vitro* studies on the two compounds were conducted including VeroE6 toxicity, anti-COVID-19 activity, determination of inhibitory activity towards papain-like proteinase (PL pro) and spike protein- and receptor- binding domain (RBD) as well as assessment of drug toxicity on RBCs.

Results The results showed that ZnO/BER complex acts as an anti-COVID-19 by inhibiting spike protein binding with angiotensin-converting enzyme II (ACE II), PL pro activity, spike protein and E protein levels, and expression of both E-gene and RNA dependent RNA polymerase (RdRp) at a concentration lower than that of BER or ZnO-NPs alone. Furthermore, ZnO/BER complex had antioxidant and antimicrobial properties where it prevents the auto oxidation of 2,2-Diphenyl-1-picrylhydrazyl (DPPH) and the culture of lower respiratory system bacteria that affected Covid 19 patients. The ZnO/BER complex prevented as well the HCQ cytotoxic effect on both RBC and WBC (*in vitro*) and hepatotoxicity, nephrotoxicity and anemia that occurred after HCQ long administration *in vivo*.

Conclusion The ZnO/BER complex can be accounted as promising anti-COVID 19 candidate because it inhibited the virus entry, replication, and assembly. Furthermore, it could be used to treat a second bacterial infection that took place in hospitalized COVID 19 patients. Moreover, ZnO/BER complex was found to eliminate the toxicity of long-term administration of HCQ *in vivo*.

Keywords COVID-19 · Papain-like proteinase · Spike protein RBD · Molecular docking analysis · ACE2 · Vero E6 toxicity · Berberine · ZnO nanoparticles

Introduction

The outbreak of potentially lethal coronavirus disease 2019 (COVID-19), which originated from wild animals and birds, has resulted in more than 2,118,416 deaths and 98,834,415 confirmed cases until 23 January 2021 (Ghareeb et al. 2021). In fact, the outer membrane of COVID-19 virus consists of spike, envelope, and nucleocapsid that surround the viral

✉ Sally A. El-Zahaby
sally.elzahaby@yahoo.com

Extended author information available on the last page of the article

RNA. Viral RNA is responsible for the expression of RNA-dependent RNA polymerase (RdRp), coronavirus 3-chymotrypsin-like protease (3CLpro), and papain-like protease (PLpro) (Liu et al. 2020a). Virus invades cells through the binding of spike protein S1 subunit with cell receptor; angiotensin-converting enzyme II (ACE2) and it can also bind to CD26 (Shang et al. 2020). In contrast, the spike protein S2 subunit is responsible for membrane fusion. The virus is entered into to host cells is *via* the clathrin (endosomal) and non-clathrin (non-endosomal) pathways. In both pathways, S1 binds to ACE2, then the endosomal pathway is facilitated by pH-dependent cysteine protease cathepsin L, while non-endosomal pathway requires an additional activation/cleavage of the S protein into S1 and S2 domains by transmembrane protease/serine subfamily member 2 and 11D (TMPRSS2 and TMPRSS11D) (Tang et al. 2020). After virus entry, the viral single-stranded positive RNA is released and then replicated by replicase polyproteins that are processed by two cysteine proteases, 3CLpro and PLpro into 16 nonstructural proteins. The 3CLpro participates in viral replication key enzymes generation (e.g., helicase and RdRp). Beside the role of PLpro in replicase polyprotein cleavage, it suppresses type I interferon production through its deubiquitylation activity, which consequently accelerates coronavirus-host innate immune system evasion, contributing to pathogenesis (Chen et al. 2020b; Taefehshokr et al. 2020).

Several studies have reported that about 14.3–28% of COVID-19 patients are coinfecting with bacteria, fungi, and viruses like *Staphylococcus aureus*, *Haemophilus influenzae*, *Streptococcus pneumoniae*, *Acinetobacter baumannii*, *Enterobacteriaceae*, *Aspergillus flavus*, *Candida glabrata*, and *Candida albicans* (Chen et al. 2020a; Contou et al. 2020; Langford et al. 2020; Sharifipour et al. 2020). For this reason, the usage of empiric antibiotic is encouraged.

According to WHO, the drug repurposing (Zhou et al. 2020) is the golden choice for COVID-19 treatment selections such as anti-inflammatories, immune suppressants, anti-neoplastic agents, selective estrogen receptor modulators, anti-viral drugs, and anti-malaria agents. Likewise as the one-year clinical trials, the only approved WHO drug is baricitinib (rheumatoid arthritis treatment) in combination with remdesivir (anti-viral) (WHO 2021). Moreover, it is mentioned that the inhibition of both viral cysteine proteases (PLpro and 3CLpro) function will block the viral replication and prevent the infection (Chen et al. 2020b; Taefehshokr et al. 2020).

Among many investigational or approved antiviral medications, chloroquine (CQ) and hydroxychloroquine (HCQ) are considered the most common anti-COVID-19 drugs that have been incorporated into treatment protocols. In fact, about 50% of oral dose of HCQ reaches the blood at maximum concentration 1 h to 2 h later.

Unfortunately, HCQ accumulates significantly in the liver and lung (700 times higher than plasma concentration) and then in brain and spinal cord tissue (30 times higher than plasma level). Although CQ and HCQ act as anti-COVID-19 through *in vitro* and *in vivo* studies, they have cardio-ocular toxicity (Zou et al. 2020). Basically, CQ and HCQ exert their anti-COVID-19 effect via preventing the viral entry by increasing intracellular pH besides interfering with the glycosylation of Severe Acute Respiratory Syndrome Coronavirus (SARS-CoV) receptors and finally inhibiting the viral replication (Liu et al. 2020b; Wang et al. 2020). According to the European Medicines Agency (2020), both CQ and HCQ can be used for the treatment without combination with other drugs or in high doses.

Berberine (BER), an isoquinoline alkaloid, has been reported to reveal some pharmacological properties including; antimicrobial activity against 54 microorganisms, intestinal ion secretion and smooth muscle contraction inhibition, hinder of ventricular tachycardia, alleviating inflammation, stimulating bile secretion and bilirubin discharge (Minaiyan et al. 2011). With regard to our previous work, we reported that BER has antioxidant, anti-inflammatory, antimicrobial, and anti-HCV properties where it acts as an NS5, RNA polymerase, indoleamine 2,3-dioxygenase (IDO), and programmed cell death protein 1 (PD1) inhibitor (Ghareeb et al. 2013; Saleh et al. 2018). Moreover, it increases INF- γ and IL-12 production, stimulates the proliferation of dendritic cells toward T-helper I class, induces cancer cell death through increasing the expression of the apoptotic markers (Caspase-3 and p53) associated with inflammatory markers down-regulation (myeloperoxidase, MAPK and COX-2), stimulates white blood cell proliferation, and it also has no cytotoxic effect toward normal cells *in vitro* and *in vivo* (Mahmoud et al. 2016; Ghareeb et al. 2016). Additionally, we verified the hepatoprotective effect of BER *in vitro* and *in vivo*. It effectively ameliorates the insulin signaling pathway in metabolic syndrome-induced rats by controlling glycemic and lipidemic profiles in addition to decreasing TNF- α and IL-6 levels (Abd El-Salam et al. 2015; Ghareeb et al. 2013, 2016, 2018; Hussien et al. 2018; Saleh et al. 2018; Soudi et al. 2019; Mahmoud et al. 2016).

Zinc oxide (ZnO), which is a potent antioxidant and anti-inflammatory compound, has demonstrated its good antibacterial activity against Gram-positive and Gram-negative bacteria. Moreover, it has shown a promising anti-viral effect against chikungunya virus, Herpes simplex virus 1 and 2 (HSV-1 and HSV-2) and also affects the replication of influenza virus (H1N1) (Ghaffari et al. 2019). Besides that, ZnO is commonly used as a food additive and it was graded as a safe substance by the US Food Administration (Espitia et al. 2016; Jiang et al. 2018).

Kim et al. (2018), proved that ZnO/Berberine nanoparticles could be used for lung cancer treatment due to its chemo-photothermal therapeutic efficacy.

To date, there is no research using ZnO nanoparticles with the complexation of berberine as antiviral agent, therefore this study is the first to consider the anti-microbial effect of ZnO/berberine complex. Based on these findings, the current study was conducted in order to estimate the efficiency of both BER and the well characterized synthetic ZnO/BER complex as an anti-COVID-19 therapy, as well as to assess their possible mechanism of action. Furthermore, the current study attempts to overcome the restrictions of current therapies to examine the compounds toxicity/safety and their aptitudes to eliminate HCQ toxicity, *in vitro* and *in vivo*.

Material and methods

Materials

Berberine chloride hydrate (>98% purity) was purchased from Sigma Aldrich, Germany. Zinc acetate dihydrates was purchased from polskie odczynniki chemiczne S.A., Poland. Sodium hydroxide pellets were obtained from Fisher Chemical, Germany. HPLC grade ethanol and methanol were purchased from Sigma Aldrich, Germany. All other chemicals were of analytical grade.

Preparation and characterization of ZnO nanoparticles and ZnO/BER complex

Preparation of ZnO nanoparticles

ZnO nanoparticles (ZnO-NPs) were synthesized using the solvo-thermal synthesis method, as reported in Aditya et al. (2019), with some modifications. Zinc acetate dihydrates (9.02 mmol) (Fisher Chemical, Germany) was first dissolved in 52.5 ml of methanol/water (16:5) solution. Subsequently, 30 ml methanol contains 17.5 mmol NaOH was drop-wisely added under vigorous stirring to the solution, followed by agitation for 30 min at room temperature. The pellets were collected by centrifugation for 15 min, at 17,500 rpm. The collected pellets were washed several times by acetone: ethanol mixture. The resulting pellets were then dried overnight in a vacuum.

Preparation of ZnO/BER complex

ZnO/BER complex was prepared by a facile mixing method as reported in Kim et al. (2018) considering the solubility of BER and dispersibility of ZnO-NPs in different solvents. First, ZnO-NPs were dispersed in milli Q water at a concentration of 5 mg/ml using a probe-type sonicator for 30 min.

Similarly, BER was dissolved in milli Q water at 5 mg/ml and sonicated in ultra-sonic cleaner bath for 10 min until complete solubility “clear bright yellow color”. Then, the ZnO-NPs suspension and BER solution were mixed and diluted with milli Q water while stirring. The mixture was then agitated at room temperature for 2 h. This mixture was concentrated using a vacuum evaporator and then completely dried by using freeze dryer to obtain the complex powder. For further use and characterization, the powder was resuspended in milli Q water.

Characterization methods to confirm the formation of ZnO/BER complex

Structural and physical characterization

Zetasizer analyses

The hydrodynamic size and polydispersity index values of ZnO-NPs and ZnO/BER complex were detected using dynamic light scattering (DLS) technique and Zetasizer Nano ZS (Malvern, Worcestershire, UK). In addition, zeta potential was measured using the same instrument (Raafat and El-Zahaby 2020).

Transmission electron microscopy and energy dispersive X-ray analysis (EDX) analyses

The morphology (shape and size) and elemental analysis of the ZnO-NPs and ZnO/BER complex were detected by transmission electron microscopy (TEM) (JEOL, JEM 1400, Tokyo, Japan) operating at an acceleration voltage of 80 kV and energy dispersive X-ray analysis (EDX) (Oxford instruments X-Max, 80mm² EDS system, UK), respectively (El-Zahaby et al. 2016).

UV/Visible analyses

Spectral analysis and UV/Visible absorption of BER, ZnO-NPs, and ZnO/BER complex aqueous suspensions were detected using UV–Vis Spectrophotometer (Thermo Scientific™ Evolution™ 300, Thermo Scientific, USA) in the range of 200–600 nm, at room temperature with a 1 cm path quartz cell.

Spectro fluorophotometer analyses

The excitation and emission spectra of the BER, ZnO-NPs, and ZnO/BER aqueous suspension were measured using a Hitachi F-2700 FL Spectro fluorophotometer, Hitachi, Japan. The fluorescence spectra were recorded at an excitation wavelength of 325 nm with the slits (Ex/Em) set at

5.0/10.0 nm. Spectra were recorded in the wavelength range of 350–600 nm using a 1 cm path quartz cell.

Fourier-transform infrared (FT-IR) analysis

FTIR spectra of the BER, ZnO-NPs and ZnO/BER complex were obtained using a Shimadzu IRTracer-100 FT-IR spectrophotometer (Shimadzu, Japan) in a KBr disk. The value was detected in the wave number of 400 cm^{-1} to 4000 cm^{-1} (Wen et al. 2021).

X-ray powder diffraction (XRD) analyses

XRD experiments were performed to evaluate the change in crystalline nature of ZnO-NPs, BER and ZnO/BER complex using Shimadzu XRD-6100 diffractometer (Shimadzu, Japan) with a copper source (1.54 \AA). Intensity (counts) values were detected in the 2θ range of $10\text{--}80^\circ$. The parameters of X-ray generator were determined as follows: 30 mA (current) and 40 kV (tension) (Dubey et al. 2018).

Quantitative and elemental analysis

HPLC and inductively coupled plasma-optical emission spectroscopy (ICP) analyses

BER and elemental Zn contents in the resulting ZnO/BER complex were quantitatively determined by using high-performance liquid chromatography (HPLC; Shimadzu HPLC LC-2010, Japan) and inductively coupled plasma-optical emission spectroscopy (ICP-OES, PerkinElmer, UK), respectively.

EDX analysis

The elemental composition of ZnO and ZnO-Ber NPs was observed by EDX technique using Oxford instruments X-Max, 80 mm^2 EDS system.

In silico analysis

First, the chemical structure of the compounds was drawn using Chem Sketch programme. This software was used to draw the structure of ligand in MOL format. Then Babel software was used to convert the format of the file from MOL file to PDB format. Protein PDB files were downloaded from www.rscb.org, then SWISS-PDBVIEWER (SPDBV) was used to co-ordinate energy minimization of the current study protein to be ready for docking. Molecular docking was performed by the software, “Auto dock 4.0 and LigPlus analysis” software where the ligand (ZnO-NPs, BER and ZnO/BER) was docked into the protein (PLpro, spike

protein and spike protein receptor-binding domain). Then Cygwin was used to create a GLG file and DLG file for running the docking algorithm and finding the minimum binding energy. Finally, UCSF Chimera software was used to visualize the docked protein and hydrogen bond analysis of the result.

Anti-SARS-CoV2 assays comparing to HCQ

Determination of compounds inhibitory activity towards papain-like proteinase, spike protein-receptor binding domain and ACE2 binding (Tai et al. 2020)

To estimate the inhibitory activity of ZnO-NPs, BER, ZnO/BER complex or HCQ towards papain-like proteinase, spike protein-receptor binding domain and ACE2, different concentrations were used as illustrated in Table 1.

Papain-like proteinase (PLpro)

40 μl volume of 142 nM PLpro in buffer A [50 mM HEPES, pH 7.5; 0.1 mg/ml bovine serum albumin (BSA), and 5 mM Dithiothreitol (DTT)] was dispensed in 96 well plat and then incubated with 100 μl of different concentrations of either BER, ZnO-NPs, or ZnO/BER complex for 5 min. Reactions were initiated by the addition of a fluorogenic substrate, Arg-Leu-Arg-Gly-Gly-AMC (Enzo Biochem, USA) (RLRGG-AMC, 10 μl of 250 μM) in buffer A, shaken vigorously for 30 s, and then incubated for 6 min. The reactions were subsequently quenched with 10 μl acetic acid (0.5 M), shaken for 30 s, and measured for fluorescence emission intensity (excitation λ : 360 nm; emission λ : 460 nm). Finally, percentage of inhibition (%) was detected.

Spike protein- receptor- binding domain (RBD)

First, SARS-CoV2, RBD (Abcam, UK) (1 $\mu\text{g/ml}$) was incubated with the tested compounds at $37\text{ }^\circ\text{C}$ for 2 h. This reaction mixture was added into 96-well plate and incubated overnight at $4\text{ }^\circ\text{C}$, then blocked with 2% fat-free milk in phosphate-buffered saline with Tween[®] detergent (PBST) for 2 h at $37\text{ }^\circ\text{C}$. The diluted ACE2 protein (Abcam, UK) was added to the plates and incubated for 2 h at $37\text{ }^\circ\text{C}$. After four washes, bound protein was detected using hACE2-specific goat antibody (0.5 $\mu\text{g/ml}$, R&D system, USA) that was incubated for 2 h at $37\text{ }^\circ\text{C}$, followed by incubation of horseradish peroxidase (HRP) conjugated anti-goat IgG antibody (1:5000, Thermo Fisher Scientific, Germany) for 1 h at $37\text{ }^\circ\text{C}$. The reaction was visualized by the addition of the substrate, 3,3',5,5'-Tetramethylbenzidine (TMB) (Sigma, St. Louis, MO, Germany) and stopped by H_2SO_4 (1 N). The

Table 1 The inhibitory/binding effect of the tested compounds on papain like proteinase, spike protein receptor binding domine and ACE2

Tested compounds	Concentration (µg/ml)	PLpro (Inhibition %)	Spike protein- RBD-complex formation (Fold change)	ACE2 (Binding %)
ZnO-NPs	104	71.06 ± 1.30	20.25 ± 0.50	16.40 ± 0.90
	52	62.20 ± 0.90	13.38 ± 0.30	15.60 ± 0.70
	26	45.60 ± 1.10	06.63 ± 0.20	13.10 ± 1.30
	13	35.31 ± 0.77	03.50 ± 0.30	10.70 ± 0.80
	6.5	22.50 ± 0.12	00.50 ± 0.02	08.20 ± 0.08
BER	1008	93.26 ± 0.73	16.13 ± 0.03	15.60 ± 1.10
	504	84.80 ± 0.12	16.13 ± 0.20	15.60 ± 1.60
	252	78.93 ± 0.36	08.50 ± 0.00	13.90 ± 1.10
	126	65.89 ± 0.17	08.00 ± 0.10	13.10 ± 0.90
	62.5	49.80 ± 0.19	03.88 ± 0.08	13.10 ± 0.07
ZnO/BER	166.5	98.10 ± 0.25	7.375 ± 0.02	15.60 ± 1.01
	83.25	90.51 ± 0.34	1.625 ± 0.05	11.50 ± 1.80
	41.63	81.80 ± 0.42	1.125 ± 0.09	10.70 ± 0.80
	20.81	77.40 ± 0.35	0.75 ± 0.008	02.60 ± 0.30
	10.41	70.80 ± 0.32	0.50 ± 0.002	00.80 ± 0.05
HCQ	200	37.00 ± 0.42	0.50 ± 0.001	15.60 ± 1.40
	100	30.00 ± 0.23	0.50 ± 0.001	14.80 ± 0.90
	50	22.50 ± 0.15	0.38 ± 0.003	14.50 ± 0.80
	25	11.20 ± 0.39	0.258 ± 0.001	13.80 ± 1.10
	12.5	08.10 ± 0.74	0.13 ± 0.007	09.02 ± 0.50

The results are mean ± SD

absorbance at 450 nm was measured by an ELISA plate reader (Tecan, San Jose, CA) and fold change of RBD-ACE2 complex formation was estimated.

ACE2 binding (confirmation test)

In a 96-well ELISA, the diluted ACE2 protein was incubated with the tested compounds at 37 °C for 2 h and then the plate was incubated overnight at 4 °C. After four washes, bound protein was detected using hACE2-specific antibody (goat 0.5 µg/ml) that was incubated for 2 h at 37 °C, followed by incubation of HRP conjugated anti-goat IgG antibody (1:5000) for 1 h at 37 °C. The reaction was visualized by addition of TMB and stopped by H₂SO₄ (1 N). The absorbance at 450 nm was measured by an ELISA plate reader (Tecan, San Jose, CA) and the binding % between ACE2 and the tested compounds was detected.

In vitro antiviral effect

VeroE6 toxicity

The tested compounds were diluted with Dulbecco's Modified Eagle's Medium (DMEM). Stock solutions of the tested compounds were prepared in 10% DMSO in ddH₂O. The cytotoxic activity was tested in Vero E6 cells by using the 3-(4, 5-dimethylthiazol -2-yl)-2, 5-diphenyltetrazolium bromide (MTT) method with slight modification. In brief, cells were seeded into 96-wellplates (100 µl/well at a density of 3 × 10⁵ cells/ml) and incubated for 24 h at 37 °C in 5% CO₂. After 24 h, cells were treated with various concentrations of the tested compounds in triplicates and incubated for 24 h. The supernatant was then discarded, and the cell monolayers were washed with sterile phosphate buffer saline (PBS), 3 times. MTT solution (20 µl of 5 mg/ml stock solution) was added to each well and incubated at 37 °C for 4 h followed

by medium aspiration. In each well, the formed formazan crystals were dissolved with 200 μ l of acidified isopropanol (0.04 M HCl in absolute isopropanol, 0.073 ml HCl in 50 ml isopropanol). The absorbance of formazan solutions was measured at λ_{max} 540 nm with 620 nm as the reference wavelength using a multi-well plate reader. The percentage of cyto toxicity compared to the untreated cells was determined by the following equation (Eq. 1):

$$\% \text{Cytotoxicity} = \frac{(\text{absorbance of cells without treatment} - \text{absorbance of cells with treatment}) \times 100}{\text{absorbance of cells without treatment}} \quad (1)$$

The plot of % cytotoxicity versus sample concentration was used to calculate the concentration which exhibited 50% cytotoxicity (IC50).

Anti-COVID-19 activity (Plaque reduction assay)

In a six-well plate where Vero E6 cells (1×10^6 cells/ml) were cultivated for 24 h at 37 °C. SARS-CoV2 was diluted to give 1×10^4 plaque-forming unit(PFU)/well and mixed with 100 μ l of the safe concentration of the tested compounds and incubated for one hour at 37 °C before being added to the cells. Growth medium was removed from the cell culture plates and the cells were inoculated with (100 μ l/well) of the tested compounds. After one-hour contact time for virus adsorption, 3 ml of DMEM supplemented with 2% agarose and the tested compounds and virus was added onto the cell monolayer, plates were left to solidify, and the plates were incubated at 37 °C until the formation of viral plaques

(3 days). Formalin (10%) was added for 2 h then plates were stained with 0.1% crystal violet in distilled water. Control wells where untreated virus was incubated with Vero E6 cells were included. Finally, the plaques were counted and the percentage reduction in plaques formation (% Reduction) in comparison to control wells was recorded according to the following Eq. (2):

$$\text{Reduction}(\%) = \frac{\text{Viral count(untreated)} - \text{Viral count(treated)}}{\text{Viral count(untreated)}} \times 100 \quad (2)$$

Antiviral activity

Vero E6 cells were seeded in 12-well tissue culture plates in DMEM containing 7% fetal bovine serum (FBS), 2 mM L-glutamine, 1 mM sodium pyruvate, 17.85 mM sodium bicarbonate, 15 mM HEPES and 0.8 mM geneticin. Cells were seeds at 37 °C, 5% CO₂ for 24 h prior to infection with SARS-CoV2 at an MOI of 0.1 in infection media (according to maintenance media but containing only 2% FBS) for 2 h. The inoculum-containing media was removed and replaced with 1 ml fresh media (2% FBS) containing different concentrations of the tested compounds (Table 2) or DMSO alone (10%) and incubated for 3 days. The cell supernatant was collected and spun

Table 2 Effect of ZnO-NPs, BER and ZnO/BER complex on SARS-CoV2 gene expression and protein levels

	Concentration (μ g/ml)	ORF gene expression	ORF gene down regulation (%)	E-gene expression	E-gene down regulation (%)	RdRp expression	RdRp down regulation (%)	E-protein inhibition (%)	Spike protein inhibition (%)
ZnO-NPs	5.48	0.55 \pm 0.001	45.29 \pm 0.9	0.736E ⁻⁵ \pm 0.1E ⁻⁶	99.9 \pm 1.2	0.001 \pm 0.0005	99.89 \pm 2.8	85.71 \pm 3.2	83.33 \pm 4.4
	2.74	0.18 \pm 0.002	81.96 \pm 0.3	0.336 E ⁻⁵ \pm 0.5E ⁻⁶	99.9 \pm 1.9	0.018 \pm 0.0003	98.20 \pm 3.1	78.57 \pm 1.5	78.89 \pm 3.7
	1.37	0.37 \pm 0.001	62.63 \pm 0.7	5.36 E ⁻⁵ \pm 0.2E ⁻⁶	99.99 \pm 0.9	0.019 \pm 0.0005	98.10 \pm 1.5	71.43 \pm 1.4	66.67 \pm 2.7
	0.685	0.47 \pm 0.001	53.35 \pm 0.2	7.36 E ⁻⁵ \pm 0.3E ⁻⁶	89.78 \pm 1.2	0.0277 \pm 0.0003	97.22 \pm 0.9	64.29 \pm 2.4	57.78 \pm 1.2
BER	20	0.13 \pm 0.008	86.69 \pm 0.1	0.0002 \pm 0.00001	99.98 \pm 3.9	0.001 \pm 0.00009	99.89 \pm 3.8	87.50 \pm 6.9	96.67 \pm 1.7
	10	0.39 \pm 0.002	60.22 \pm 0.8	0.003 \pm 0.0001	99.70 \pm 4.5	0.050 \pm 0.0003	94.95 \pm 6.9	50.00 \pm 4.1	94.00 \pm 2.1
	5	0.79 \pm 0.003	21.54 \pm 0.2	0.007 \pm 0.0005	99.30 \pm 1.8	0.207 \pm 0.002	79.26 \pm 3.5	25.00 \pm 0.9	86.60 \pm 1.5
	2.5	0.88 \pm 0.001	11.73 \pm 0.1	0.102 \pm 0.0003	89.77 \pm 3.5	0.233 \pm 0.001	76.67 \pm 2.9	12.50 \pm 0.8	80.00 \pm 0.8
ZnO/BER	1.665	0.12 \pm 0.001	87.71 \pm 0.1	0.009 \pm 0.00001	99.10 \pm 1.9	0.030 \pm 0.001	97.00 \pm 8.4	87.50 \pm 6.7	93.70 \pm 5.3
	0.833	0.13 \pm 0.001	86.82 \pm 0.5	0.010 \pm 0.0003	99.00 \pm 0.9	0.065 \pm 0.0003	93.50 \pm 6.3	62.50 \pm 5.4	87.50 \pm 1.8
	0.416	0.14 \pm 0.001	85.87 \pm 0.2	0.026 \pm 0.0002	97.40 \pm 8.7	0.0865 \pm 0.0002	91.34 \pm 4.8	37.50 \pm 3.1	75.00 \pm 2.8
	0.208	0.27 \pm 0.001	72.89 \pm 0.1	0.200 \pm 0.0009	80.00 \pm 3.2	0.1000 \pm 0.009	90.00 \pm 1.7	12.50 \pm 1.1	62.50 \pm 3.2

The results are mean \pm SD

for 10 min at 6000 rpm to remove debris and the supernatant was transferred to fresh collection tubes. The cell monolayers were collected by scraping and resuspension into 1 ml fresh media (2% FBS). Both supernatant and suspended cells were deactivated to kill virus particles by UV, and then several sawing and freezing steps was carried out to lysis cells (Caly et al. 2020; Xia et al. 2020).

Generation of SARS-CoV2 cDNA

RNA was extracted from 200 µl aliquots of sample supernatant or cell suspension using the Qiagen viral RNA-isolation kit (#52906). Reverse transcription was performed by the commercial first strand cDNA synthesis kit (Thermo Scientific, USA) and conducted according to the manufacturing instructions.

Detection of SARS-CoV2 gene expression using a TaqMan real-time RT-PCR assay

The amplification of BetaCoV RdRp gene and BetaCoV E-gene was carried out using the following sets of primer and probes. Regarding BetaCoV RdRp gene, 1 µM Forward (5'-AAA TTC TAT GGT GGT TGG CAC AAC ATG TT-3'), 1 µM Reverse (5'-TAG GCA TAG CTC TRT CAC AYT T-3') primers and 0.2 µM probe (5'-FAM-TGG GTT GGG ATT ATC-MGBNFQ-3') (Abcam, UK) were used. With respect to BetaCoV E-gene, 1 µM Forward (5'-ACA GGT ACG TTA ATA GTT AAT AGC GT -3'), 1 µM Reverse (5'-ATA TTG CAG CAG TAC GCA CAC A-3') primers and 0.2 µM probe (5'-FAM-ACA CTA GCC ATC CTT ACT GCG CTT CG-286 NFQ-3') (Abcam, UK) were used. The calculated Ct values were converted to a fold-reduction of treated samples compared to the control using the ΔCt method (fold changed in viral RNA = 2^{ΔCt}) and expressed as a percentage of the DMSO sample alone.

Detection of Spike protein and envelope protein

The protein level of spike protein and envelope protein was analyzed by ELISA technique using rabbit SARS-CoV2 spike polyclonal antibody and SARS-CoV2 envelope antibody (Abcam, UK), respectively. First, 100 µl of spike and envelope proteins (100 µg) were added to the well plate and incubated for 2 h at room temperature and then overnight at 4 °C. The solution was removed then 200 µl of BSA was added to the well plate and incubated for 1 h at 37 °C. After three-time wash with PBS, rabbit SARS-CoV2 spike or envelope polyclonal antibodies were added to the wells and incubated for 1 h at room temperature. After three-time wash with PBS, HRP conjugated anti-rabbit IgG antibody was added to the wells and incubated for 1 h at room

temperature. The reaction was visualized by the addition of a chromogenic substrate (TMB) and stopped by H₂SO₄ (1 N). The absorbance was measured at 450 nm by an ELISA plate reader (Tecan, San Jose, CA).

In vitro assays of biological activities of the tested compounds compared to HCQ

Red blood cells toxicity

First, a serial dilution of BER, ZnO-NPs, ZnO/BER complex and HCQ was prepared in 0.9% NaCl ranging from 2 µg/ml to 1000 µg/ml. Then, 100 µl of 1% human red blood cells suspension was added to a new microtube containing 900 µl dilutions of each compound tested and incubated at 37 °C for 1 h. After that, the tubes were centrifuged at 3000×g for 5 min. The supernatant (200 µl) was placed in a 96-well plate and the absorbance was measured at 540 nm using a microplate reader. "For positive (100% haemolysis) and negative (0% haemolysis) controls", the cells suspension of human red blood cells (100 µl) were mixed with distilled water or 0.9% NaCl (900 µl), respectively. The percentage of haemolysis was calculated as the following Eq. (3):

$$\text{Hemolysis (\%)} = \frac{(Abs_{sample} - Abs_{C-})}{(Abs_{C+} - Abs_{C-})} \times 100 \quad (3)$$

where, Abs_{sample} was the absorbance of different tested compounds, Abs_{C+} was the absorbance of positive control (100% hemolysis) and Abs_{C-} was the absorbance of negative control (0% haemolysis). All samples were assayed in triplicates. Finally, the inhibitory or effective concentration (IC₅₀/EC₅₀) which had 50% anti-hemolytic powerful and caused 50% red blood cells hemolysis was estimated in µg/ml.

Peripheral blood mononuclear cells toxicity

Peripheral blood mononuclear cells (PBMC) were collected from healthy individuals on heparinized tubes (10 U/ml) and PBMC were collected by density gradient centrifugation using sterile lymphocyte separation medium (Ficoll-Paque premium, density 1.077 g/ml, GE Healthcare, USA). Cell count and viability were determined using trypan blue exclusion test. Finally, the separated PBMC was suspended at 1.0 × 10⁵ cell/ml in Roswell Park Memorial Institute (RPMI) 1640 medium (Lonza, USA) supplemented with 25 mM N-2-hydroxyethylpiperazine-N'-2-ethanesulfonic acid (Lonza), 4 mM L-glutamine (Lonza), 100 U of penicillin and 100 µg streptomycin (Cambrex) and 10% FBS (Lonza). PBMC was incubated with different concentrations of the tested compounds.

All samples were assayed in triplicates. Proliferation was assessed using a neutral red uptake assay (Repetto et al. 2008) after incubation for 24 h at 37 °C, 5% CO₂, and 95% humidity. Finally, IC50 was calculated in µg/ml.

Antioxidant activity

The free radical scavenging activity of the tested compounds was measured by 2,2-Diphenyl-1-picrylhydrazyl (DPPH, Sigma, Germany) assay as proposed by Brand-Williams et al. (1995), with some modifications. A solution of 0.2 mM DPPH in methanol (0.0078 g/100 ml) was prepared and 100 µl of this radical solution was added to 100 µl of the tested compounds at different concentrations. The mixture was incubated in the dark for 30 min at room temperature. For control (no radical scavenging activity), 100 µl of distilled water was used instead of the tested compounds. Then the absorbance of samples (Abs_{Sample}) and control ($Abs_{control}$) was measured at 517 nm using a microplate reader. The percentage of DPPH radical-scavenging activity was calculated using the following equation, Eq. (4):

$$\text{DPPH radical scavenging activity (\% Inhibition)} = \frac{(Abs_{Control} - Abs_{Sample})}{Abs_{Control}} \times 100 \quad (4)$$

Antimicrobial activity

Antimicrobial activity was performed by using agar well diffusion assay and turbidity assay (Kadaikunnan et al. 2015) for all samples. Four microbial species known to be pathogenic including gram negative bacteria (*klebsila pneumonia ATCC700603*), gram positive bacteria (*Staphylococcus aureus ATCC25923* and *Streptococcus pyogenes EMCC1772*) and yeast (*Candida albicans EMCC105*) were tested. Strains were grown in nutrient broth at 37 °C for 24 h. A set of 5 concentrations of the tested reconstituted compounds were examined to determine the minimum inhibitory concentration (MIC) of each against a specific pathogenic strain.

Agar well diffusion assay

One hundred microliters of inoculums (1×10^8 CFU/ml) were inculcated on agar media and poured into the petri plate. A well was prepared in the plates with the help of a cork-borer (0.5 cm) and 100 µl of the tested compounds were applied into the well. All tested bacterial were incubated at 37 °C for 24 h. The inhibition zone was calculated by measuring the diameter around the well (mm), excluding

the well diameter. The readings were taken in three different fixed directions in all triplicates and the average values were tabulated.

Turbidity assay

MIC of samples was performed using the microdilution method. Briefly, cultures of bacteria broth were suspended overnight in Mueller Hinton (MH) broth with turbidity adjusted to 0.5 McFarland, resulting in a suspension containing approximately 1×10^8 CFU/ml. To measure the MIC, 50 µl of MH broth culture was poured into 12 wells of a 96-well microtiter plate. In the first well, 50 µl of the samples stock solution was added. A twofold dilution was then made to obtain a different concentration of samples in each well (µg/ml). Then 50 µl of the microbial suspension was added to each well. The microplate was then incubated at 37 °C for 24 h, and the sample concentration in the well without visible growth of the bacterial cells was considered to be MIC. The positive control (maximum bacterial growth) contained MH broth medium only with tested bacterial concentration and a negative control contained only inoculated broth were used in the study. The test was carried out in comparison

with 10 mg/ml amoxicillin. The optical density was measured at 600 nm. MIC was defined as the least concentration of the sample that visually inhibited the bacterial growth after 24 h of incubation. MIC was reported by observing the visual turbidity of the tubes before and after incubation. Bacteria inhibition (%) was calculated as the following Eq. (5):

$$\text{Inhibition (\%)} = \frac{(Abs_{Control} - Abs_{Sample})}{Abs_{Control}} \times 100 \quad (5)$$

The elimination of HCQ toxicity

In vitro assay

Red blood cells toxicity

One hundred microliters of 1% red blood cells suspension was added to 450 µl of dilution of each tested compound that gave the lowest haemolytic activity and incubated at 37 °C for 30 min. After that, 450 µl of HCQ (27.5 µg/ml) was added to all of test compounds and re-incubated for another 30 min. After that, the supernatant (200 µl) was placed in a

96-well plate and the absorbance was measured at 540 nm using a microplate reader. Finally, the percentage of haemolysis was calculated as previously mentioned in 2.5.1.

White blood cells toxicity

The blood sample (10 ml) was centrifuged at 1650 rpm for 10 min and pellets were collected. Then lysis buffer (10 times of pellet volume) was added to the pellet and centrifuged for 30 min at 1650 rpm. The supernatant was discarded, and the white pellet was resuspended in one ml RPMI 1640 medium (Lonza, USA). Cell count and viability were determined using trypan blue exclusion test. Finally, the separated WBCs were suspended at 1×10^5 cell/ml in RPMI 1640 medium supplemented with 25 mM N-2-hydroxyethylpiperazine-N'-2-ethanesulfonic acid (Lonza), 4 mM L-glutamine (Lonza), 100 U of penicillin and 100 μ g streptomycin (Cambrex) and 10% FBS (Lonza). Cells (100 μ l) were incubated with 100 μ l of different concentrations of the tested compounds for 24 h at 37 °C, 5% CO₂, and 95% humidity. After that, media were changed with media contained 200 μ g/ml HCQ and the cells was incubated for another 24 h. All samples were assayed in triplicates. Proliferation was assessed using neutral red uptake assay (Repetto et al. 2008).

In vivo assay

Thirty-six male albino mice weighing 20–25 g were purchased from the Theodor Bilharz Research Institute, Cairo, Egypt. Mice were housed in an animal facility of Pharmaceutical and Fermentation Industries Development Centre (PFIDC), SRTA-City. Animals were housed 6 mice/cages under controlled temperature (25 ± 2 °C) and constant photoperiodic conditions (12:12-h daylight/darkness). Mice were allowed free access to water and a balanced commercial chow. The animal experiment design protocol was approved by ethics committee of animal research in (PFIDC), SRTA-City, Institutional Animal Care and Use Committees (IACUC)/IACUC # 19-1R-01020.

The animals were divided into six groups. The first 3 groups received orally 250 μ l of either milliQ water (control), BER solution (100 mg/kg, BER group) and ZnO/BER solution (3.3 mg/kg, ZnO/BER group). The second 3 groups received the previous treatments in combination with 250 μ l of HCQ solution (36 mg/kg) and named after the HCQ, HCQ + BER and HCQ + ZnO/BER groups, respectively. All the treatments are dissolved in milliQ water and continued for 28 days.

At the end of the experimental period, mice were fasted overnight, and then anesthetized with sodium pentobarbital (100 mg/kg i.p.) to minimize animal suffering. Blood

samples were collected in heparinized test tubes. After complete blood picture (CBC) determination, plasma was isolated by centrifugation and sera were collected to measure routine blood chemistry.

CBC was analyzed using an automated hematology analyzer (BC-2800Vet-Mindray, China) as well as blood parameters (alanine aminotransferase (ALT), aspartate aminotransferase (AST) and alkaline phosphatase (ALP) activities as well as total protein, albumin, bilirubin, triglyceride (TG), creatinine, uric acid and urea levels) were measured using a clinical chemistry analyzer (BS-230-Mindray, China) according to commercial kit manufacturing instructions.

Statistical analysis

SPSS software package version 20.0 (Armonk, NY: IBM Corp) was used for data analyses. Data are presented as mean and standard deviation, significance among groups at $p < 0.05$ was assessed by using ANOVA and post hoc LSD test.

Results and discussion

Characterization of ZnO nanoparticles and ZnO/BER complex

UV–vis spectral analysis (Fig. 1a) shows that the characteristic absorption peak for wurzite hexagonal ZnO-NPs was found at 372 nm (Estrada-Urbina et al. 2018). While the absorbance at 228, 260, 344 and 420 nm is the characteristic absorption peaks for berberine chloride. In ZnO/BER complex spectrum, the characteristic absorption peaks were like BER alone. Moreover, the ZnO-NPs specific absorption peak was hidden and there was a slight broadening and increase in the absorbance intensity peak at 420 nm of BER in ZnO/BER complex spectrum (Fig. 1b and c). These effects are may be due to the absorption of BER on the surface of ZnO-NPs and the formation of ground state complex formed by ZnO/BER complex interaction (Bhogale et al. 2013) and formation of ZnO/BER complex aggregates.

The fluorescence intensities of BER aqueous solution in the range of 350–600 nm which presented in Fig. 1d shows a pair of very low fluorescence intensity at $\lambda_{\max} = 370$ nm and $\lambda_{\max} = 540$ nm respectively. The fluorescence spectrum of the ZnO-NPs aqueous suspension exhibits most of the ZnO-NPs characteristic emission peaks at 378 nm, 455 nm, and 534 nm (Irimpan et al. 2007). The fluorescence intensities of the ZnO/BER complex shows the quenching of the ZnO band emission peaks at $\lambda_{\max} = 378$ nm by 48.32% with 2 nm shifting to $\lambda_{\max} = 380$ nm. Moreover, the fluorescence intensity peaks at 455 nm and 534 nm still has the same intensity with shifting 11 and 1 nm, respectively. However,

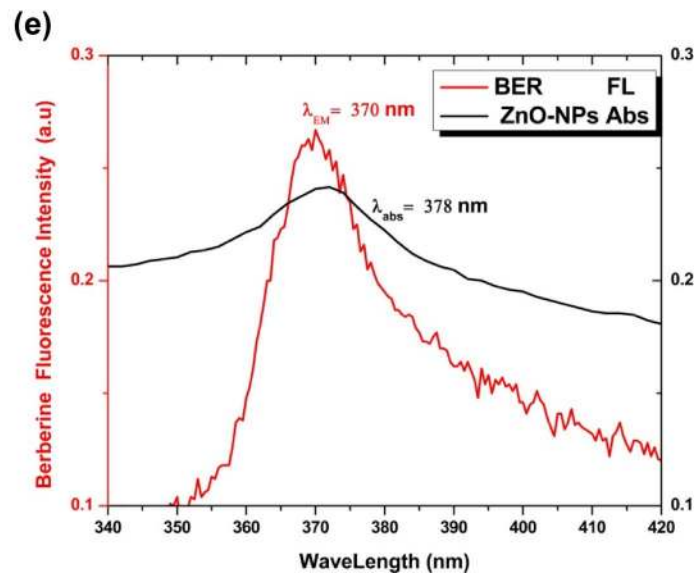
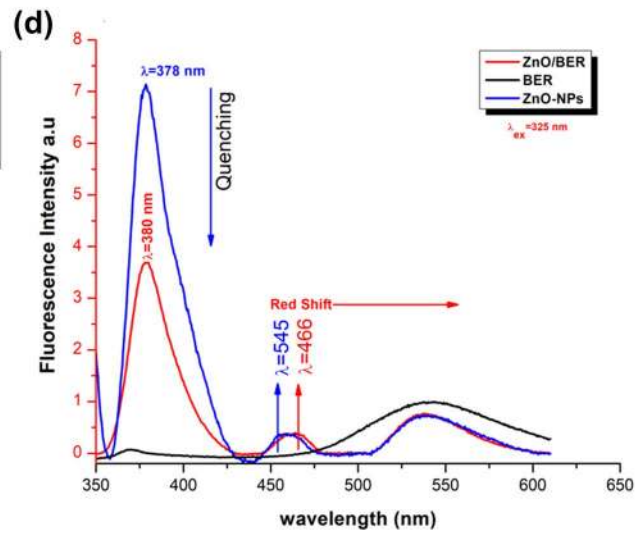
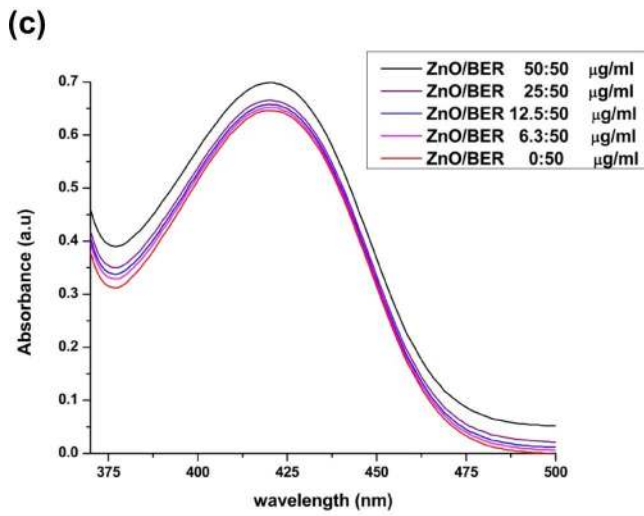
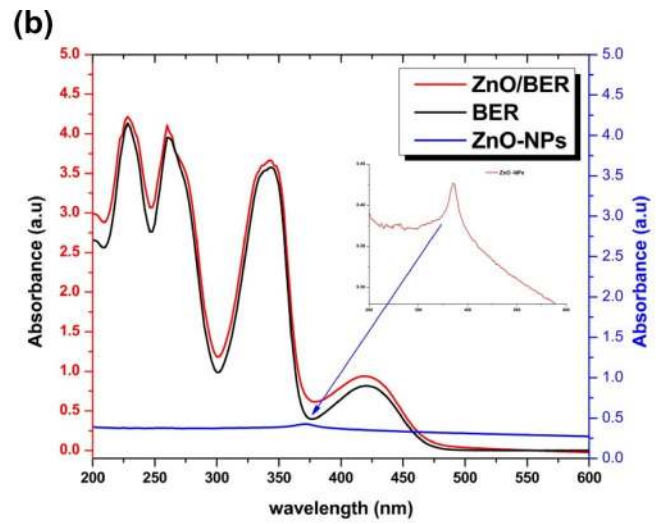
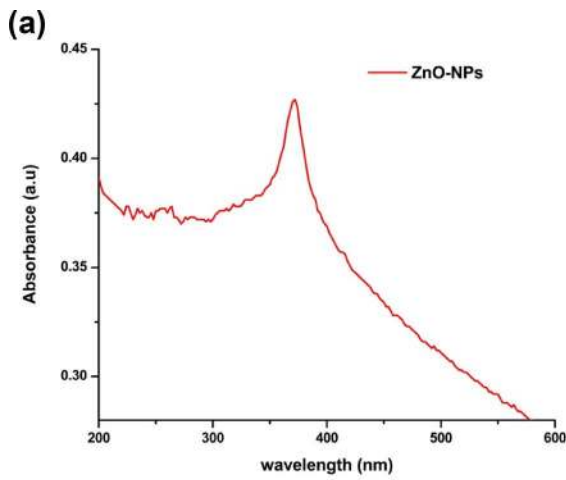


Fig. 1 Absorption spectrum of **a** ZnO-NPs suspension (104 $\mu\text{g/ml}$), **b** BER (62.5 $\mu\text{g/ml}$, *Black*) and ZnO/BER-NPs (166.5 $\mu\text{g/ml}$, *Red*) and ZnO-NPs (104 $\mu\text{g/ml}$, *Blue*) and **c** BER and ZnO/BER peaks at 420 nm with different ZnO-NPs concentration. **d** The fluorescence emission spectrum at λ excitation = 325 nm of the prepared materials suspended in milli Q water at room Temperature. BER (62.5 $\mu\text{g/ml}$, pH = 7.5, *Black*) and ZnO/BER (166.5 $\mu\text{g/ml}$, PH = 7.21, *Red*) and ZnO-NPs (104 $\mu\text{g/ml}$, pH = 7.45, *Blue*). **e** Overlap of the fluorescence emission spectrum of BER with the absorption spectrum of ZnO-NPs

in the presence of colloidal ZnO-NPs, the emission peaks of the BER band around 370 nm and 540 nm were hidden in ZnO-BER spectrum. This generally occurs due to passivation of ZnO-NPs surface and the energy transfer interaction that appears in the overlap of the emission spectrum of the donor with absorption spectrum of the acceptor (Belay et al. 2017; Jia et al. 2014; Kathiravan et al. 2009). Figure 1e clearly shows that fluorescence emission spectrum of BER overlapped with the absorption spectrum of ZnO-NPs, indicating energy transfer from the excited state of BER to ZnO-NPs resulting in the formation of ZnO/BER complex at lower energy.

Figure 2 shows that the average hydrodynamic size of ZnO-NPs was approximately 448 nm due to their tendency to aggregate in aqueous suspension, whereas the average hydrodynamic size of ZnO/BER complex was approximately 583 nm. The polydispersity index (PDI) and zeta potential of ZnO-NPs was 0.255 mv and -25.5 mv, respectively while the ZnO/BER complex was 0.32 mv and -3.71 mv, respectively. This result is due to the interaction between the negative ZnO-NPs and the cationic BER molecules which affects the polydispersity index and increases the tendency to aggregate due to the low surface potential of the complex (Liu et al. 2018).

Figure 3a shows that ZnO-NPs are highly uniformly dispersed NPs with a particle size of 30 ± 5 nm with the presence of some larger agglomerated particles. Moreover, the EDX elemental analysis of ZnO-NPs (Fig. 3c) showed that Zn and O are the main constituents in the sample and there were no traces of another element. TEM analysis of the ZnO/BER complex (Fig. 3b) showed that there were ZnO-NPs agglomerated clusters shield with a light organic layer of BER with a particle size of 65 ± 6 nm. The size was increased as the aggregates of the ZnO/BER complex were formed and this may explain the increased hydrodynamic size and the PDI of ZnO/BER complex sample. Furthermore, the EDX elemental analysis of the ZnO/BER complex (Fig. 3d) shows the presences of C, Zn and O only. Additionally, Fig. 3c shows that the content of BER in ZnO/BER complex was $(67.068 \pm 2.43 \mu\text{g/ml})$, while the Zn content was $79.55 \mu\text{g/ml}$.

To verify the intermolecular interactions between BER and ZnO-NPs in the ZnO/BER complex, infrared absorption

spectra of ZnO-NPs, BER, and ZnO/BER complex were observed in the wavenumber range from 4000 cm^{-1} to -400 cm^{-1} (Fig. 4a). The FT-IR of ZnO-NPs and BER was identical to the data published by Nagaraju et al. (2017) for ZnO-NPs and Bashmakova et al. (2011), Battu et al. (2010), Strekal et al. (2007) for BER. The FT-IR spectrum of the ZnO/BER complex shows a significant vibration band in the range of $400\text{--}500 \text{ cm}^{-1}$ which is a characteristic stretching mode of the Zn–O divalent bond at 427 cm^{-1} and surface hydroxyl residue -O–H stretching mode in the range of $3000\text{--}3600 \text{ cm}^{-1}$ (at 3405 cm^{-1}). The $\text{CH}_2\text{--O--CH}_2$, the BER ether group vibration peak (923 cm^{-1} and 1032 cm^{-1}) (Bashmakova et al. 2011) appeared with lower absorption intensity with a red shift at 903 and 1034 cm^{-1} . While the BER– OCH_3 methoxy group rocking and stretching vibration peak at 1270 cm^{-1} and 1390 cm^{-1} (Strekal et al. 2007) with lower absorption intensity at 1270 cm^{-1} peak and enhanced absorption intensity at 1390 cm^{-1} peak. This may be due to the overlapping with $-\text{OCH}_3$ methoxy group over the surface of ZnO from the synthesis precursors. Also, The BER iminium ($\text{C}=\text{N}^+$) double bond peak at 1627 cm^{-1} (Battu et al. 2010) experiences a dramatic change. It disappeared in the ZnO/BER complex spectrum, and the -C–N vibration peak of BER at 1141 cm^{-1} and 1567 cm^{-1} could not be noticed. Moreover, the existence of aromatic ring stretching vibrations of C–C, $\text{C}=\text{C}$ at 1331 cm^{-1} , 1558 cm^{-1} , 1506 cm^{-1} and 1600 cm^{-1} . The FT-IR spectrum of the BER and ZnO/BER complex showed that the BER– OCH_3 methoxy group, -C–N, iminium ($\text{C}=\text{N}^+$) double bond peak and $\text{CH}_2\text{--O--CH}_2$ ether pair peaks experienced a dramatic change in shape, transmittance (%) and band position. It implies the interactions between the principal functional groups of BER and ZnO in the ZnO/BER complex.

The structure type identification and crystallinity of ZnO-NPs, BER and ZnO/BER complex showed that the XRD pattern (Fig. 4b) of prepared ZnO-NPs has sharp and intense diffraction peaks at 2θ of 31.516° , 34.168° and 36.002° correspond to 100, 002, 101 planes where these are characteristic peaks of polycrystalline hexagonal wurzite ZnO. Furthermore, The XRD pattern of BER shows sharp and intense diffraction peaks at 2θ of 8.8452° , 26.0359° and 25.1644° , which indicates the crystalline nature of BER. The XRD pattern of the prepared ZnO/BER complex shows sharp and intense diffraction peaks for ZnO-NPs at 2θ of 31.6647° , 34.3182° and 36.1569° , in addition to the presence of less intense diffraction peaks of BER indicating the presence of less crystalline (semi-crystalline) form of BER on the surface of ZnO-NPs. The average size of the nanoparticles is calculated using Debye–Scherrer equation; $D = 0.9\lambda/\text{Cos } \theta$ equation, which was estimated of 30 ± 5 nm.

The proposed structure of the formulated ZnO/BER complex is illustrated in (Fig. 4c). The electrostatic interaction between the negatively charged ZnO-NPs and the

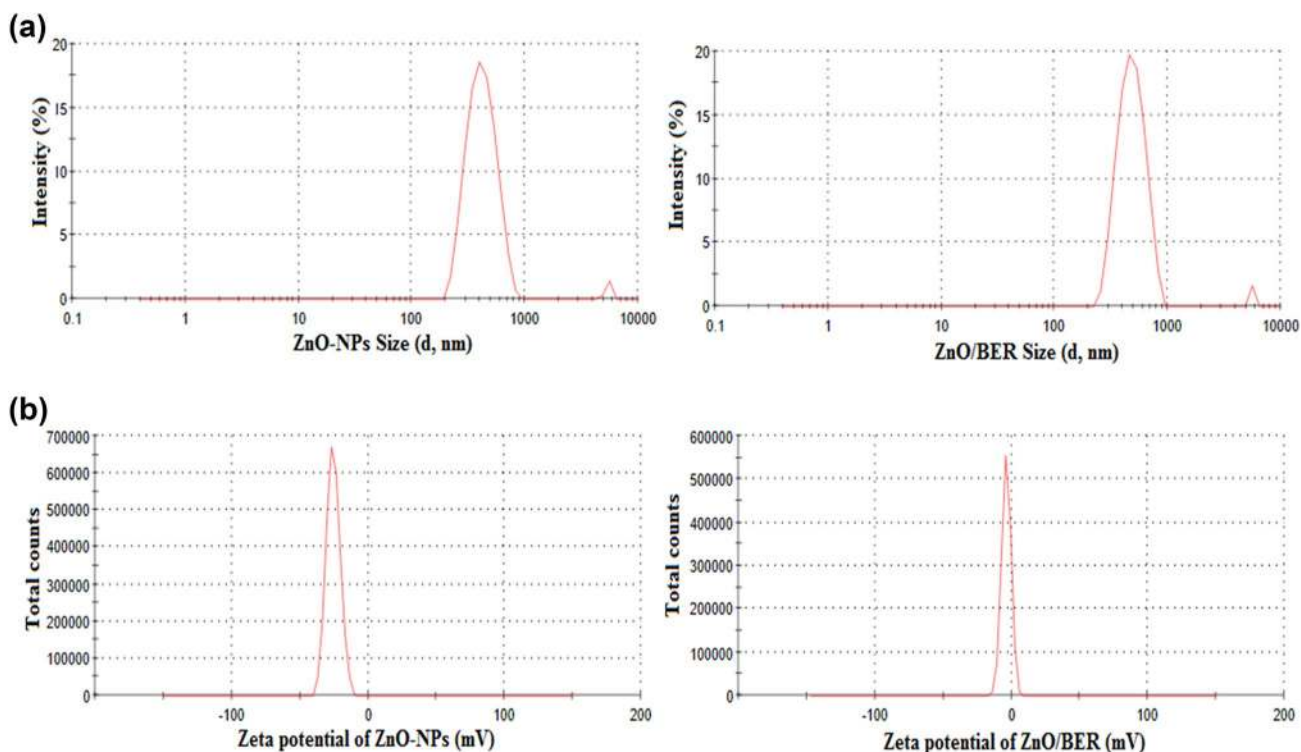


Fig. 2 **a** Hydrodynamic size (nm) of ZnO-NPs (448 nm) and ZnO/BER -NPs(583 nm) suspensions. **b** Zeta potential in (mv) of ZnO-NPs (-25.5 mv) and ZnO/BER (-3.71 mv)

cationic BER molecules affects the polydispersity index and increases the aggregation of ZnO/BER complex due to the low surface potential of the complex. Hydrogen bonding also may play a role in the formation of the ZnO/BER complex where one pair of hydrogen-bond interactions occurs by the hydrogen-bond donors acetal-type $-\text{CH}_2-$ group of the 1,3-dioxole ring in BER, which is responsible for BER crystal structure with ZnO (Pingali et al. 2014; Biradha 2003). The hydrogen bond between this $-\text{CH}_2-$ group and the oxygen of ZnO or dissociated hydroxyl $-\text{OH}$ groups could be formed on the surface of ZnO-NPs, which reduced the intense sharp peak of ZnO-NPs emission spectra at 378 nm (Fig. 1d). Another possibility of hydrogen bond is between the methoxy O atom of BER and ZnO in which the Zn atom is coordinately bonded to both methoxy O atom as shown in Fig. 4b. Additionally, the XRD pattern (Fig. 4b) of the prepared ZnO/BER complex shows the presence of less intense diffraction peaks of BER that also indicates the presence of amorphous or semi-crystalline form of BER on the surface of ZnO-NPs.

The molecular docking study.

In silico analyses of the tested compounds proved that BER binds with spike protein through BER O atom that interacts with N-atom of Gln1036 (central helix region). BER also

interacts with PLpro and spike protein RBD through hydrophobic interaction (Table 3 and Fig. 5). Whereas, ZnO-NPs bind through an O atom with spike protein active site (Asp 775 and Thr 778) and spike protein RBD through Tyr 183 and Val 506. Finally, ZnO/BER complex binds with PLpro through O with O-atom in Asp 77 and Glu 78. Furthermore, it binds with the spike protein through its O atom with O-atom of Ile666 and Pro862 and binds to the spike protein RBD through the hydrophobic interaction. Additionally, Table 3 shows that ZnO/BER complex had the lowest estimated K_i of the three examined proteins and had the highest stability as it showed the lowest binding energy value.

Antiviral effect of ZnO/BER complex

Table 1 shows that all the tested compounds had inhibitory activities towards PLpro and increased formation of the RBD spike protein complex. The results indicated that the ZnO/BER complex inhibits the spike protein in a non-competitive manner. Furthermore, they had the ability to bind to ACE2 protein (spike protein RBD). In particular, the ZnO/BER complex was the most potent inhibitor towards PLpro followed by BER, ZnO-NPs, and finally HCQ (Table 1). Furthermore, the ZnO/BER complex showed the highest inhibitory action towards RBD spike protein followed by HCQ, ZnO-NPs, and finally BER (Table 1).

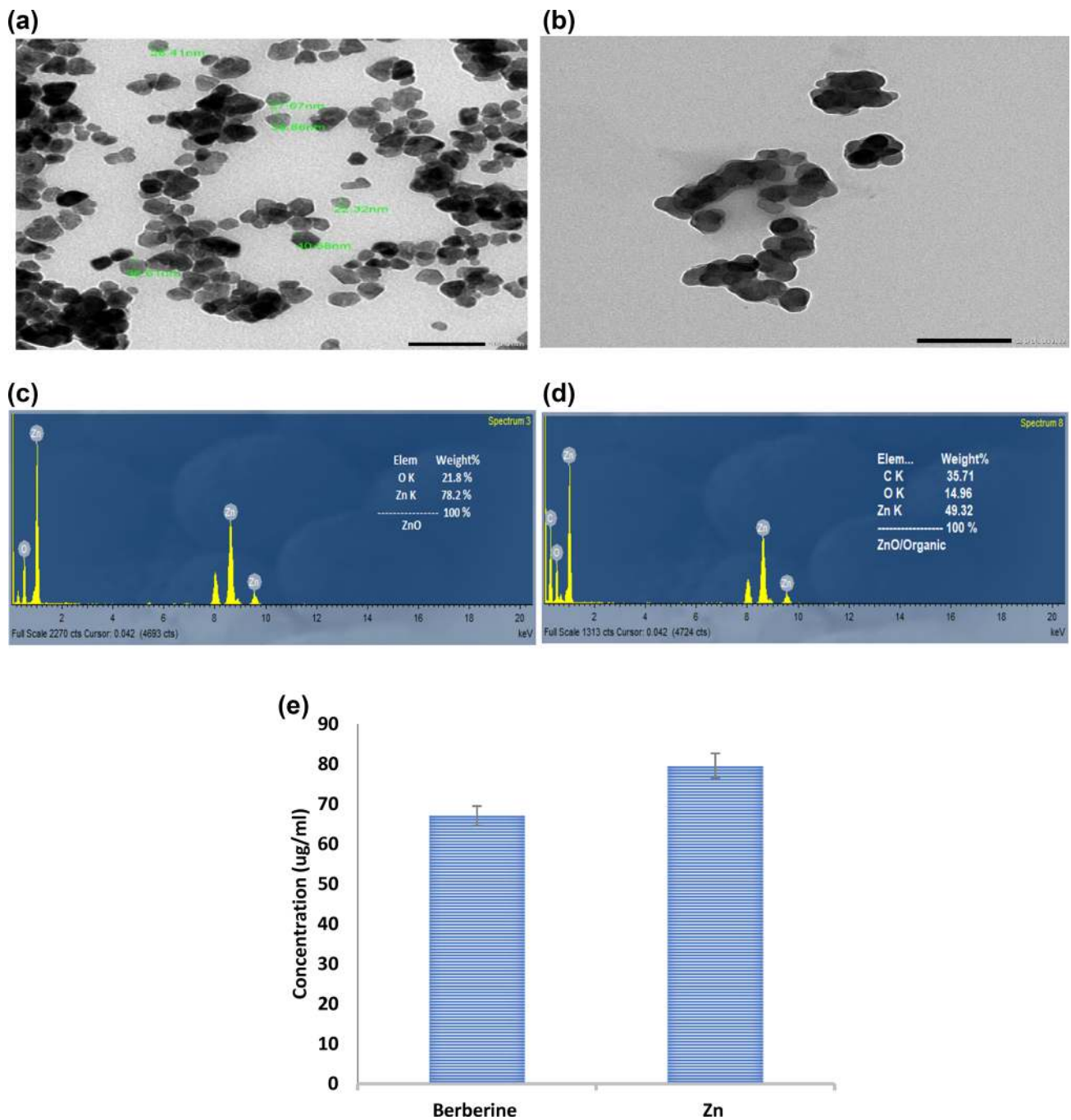


Fig. 3 TEM images of ZnO-NPs **a** and ZnO/BER-NPs **b**, Energy Dispersive X-ray analysis (EDX) **c**, **d** of ZnO-NPs and ZnO/BER, respectively. **e** Quantitative determination of both the BER and elemental Zn content in ZnO/BER complex using high-performance liquid chromatography

The current findings revealed that all the tested compounds act as anti-SARS-CoV2 as all tested compounds decreased the plaque formation % (Table 4). Remarkably, the best compound used was the ZnO/BER complex followed by BER, HCQ, and finally ZnO-NPs. In addition, all the tested compounds exhibited a potent antiviral effect as the EC_{50} (effective antiviral concentration 50) of any of the tested

compounds was lower than IC_{50} (Vero E6 inhibitory concentration 50).

Table 2 demonstrates one of our nos results that the ZnO-NPs, BER and ZnO/BER complex inhibited ORF, E- and RdRp- gene expression. Interestingly, the inhibition pattern was concentration dependent. Consequently, these results are consistent with the inhibition levels of E-protein and spike protein considering that the ZnO/BER complex had

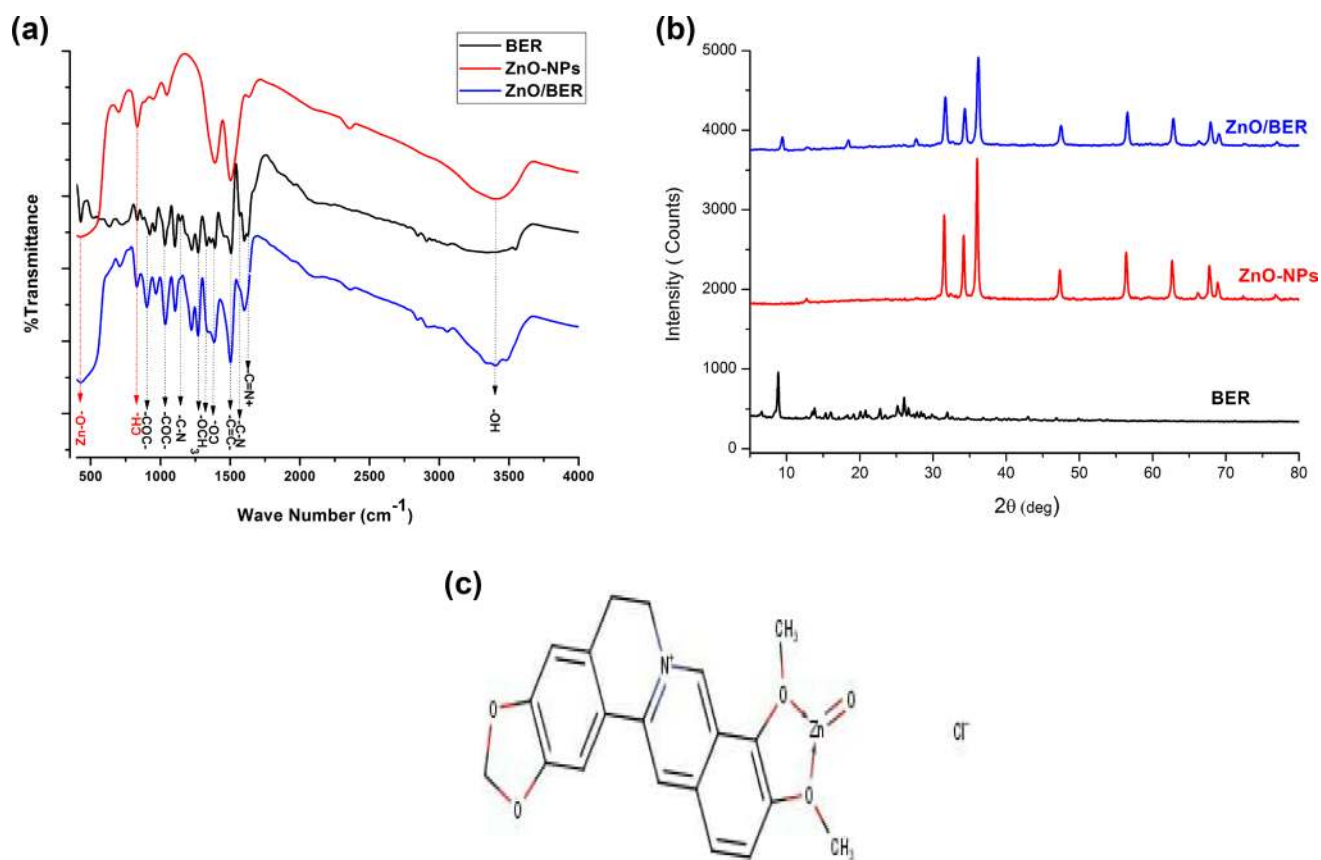


Fig. 4 FT-IR spectral analysis **a**, X-ray diffraction **b** of the ZnO-NPs, BER and ZnO/BER complex and **c** the proposed structure of the ZnO/BER complex

Table 3 Docking results of the tested compounds with papain-like proteinase, spike protein and spike protein receptor-binding domain

Parameters	BER	ZnO-NPs	ZnO/BER
pH	2.73	6.75	3.5
<i>Papain-like proteinase</i>			
Hydrogen bond	No hydrogen bond	No hydrogen bond	LIG 1 O Asp77.A O LIG 1 O Glu78.A O
Binding energy	-8.64	-2.77	-10.48
Estimated K _i	464.26 nM	9.28 mM	11.38 nM
<i>Spike protein</i>			
Hydrogen bond	Gln1036. BN-LIG O	LIG1O-Asp775.C OD1 LIG1O-Thr778.C-OG1	LIG 1 O Ile666.A O LIG 1 O Pro862.B O
Hydrophobic bonds			
Binding energy	-7.76	-2.74	-10.61
Estimated K _i	2.05 μM	9880 μM	16.64 nM
<i>Spike protein receptor-binding domain</i>			
Hydrogen bond	No hydrogen bond	LIGO-Tyr183.A OH LIGO-Val506.A O	LIG Zn-Glu402 A OH LIG Zn-His378 A NH2
No hydrogen bond			
Binding energy	-8.51	-2.31	-10.77
Estimated K _i	0.58097 μM	20,180 μM	12.85 nM

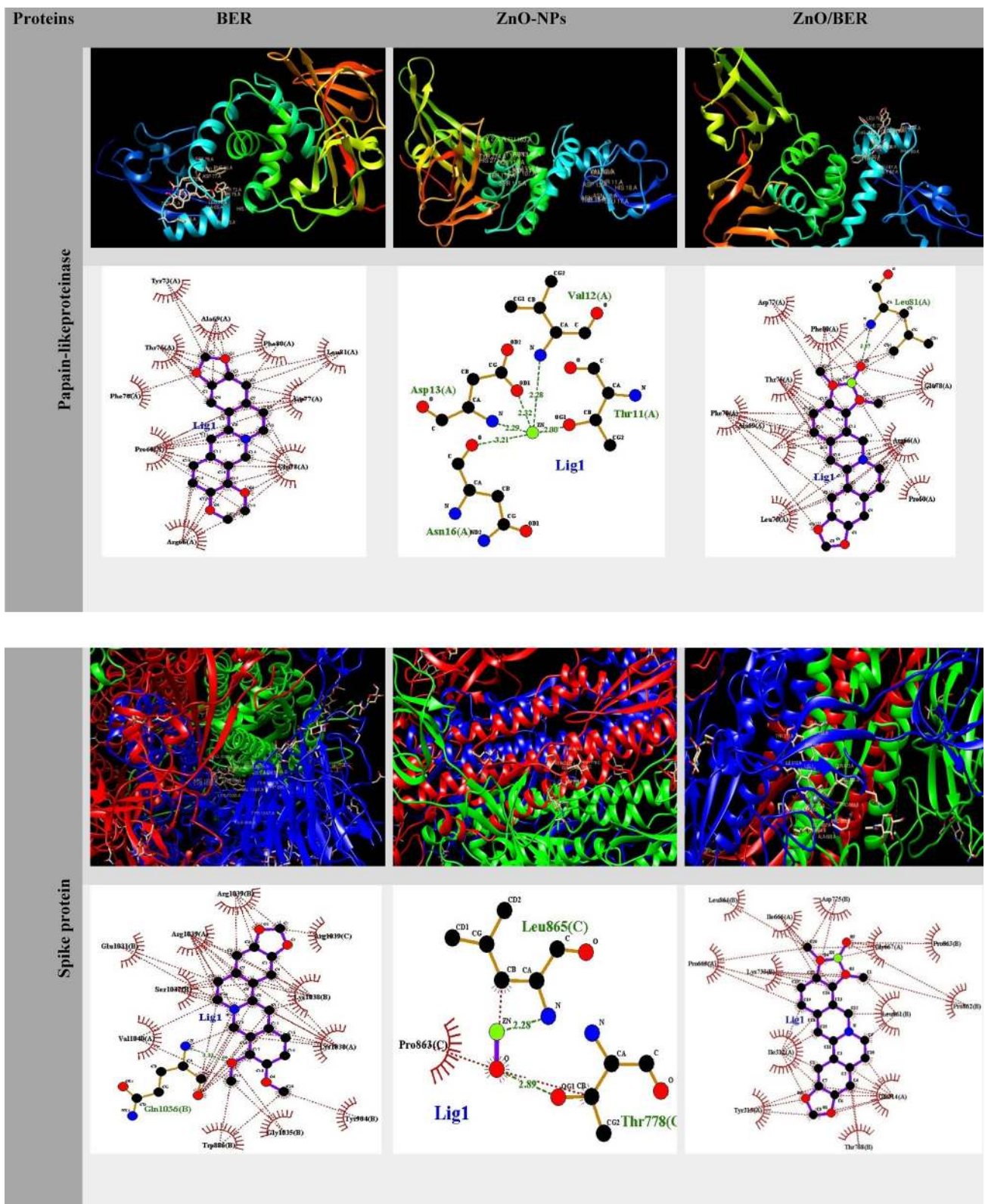


Fig. 5 Molecular docking and LigPlus analysis illustrating the interaction between ZnO-NPs, BER and ZnO/BER-NPs and the studied proteins (papain-like proteinase, spike protein and spike protein receptor-binding domain)

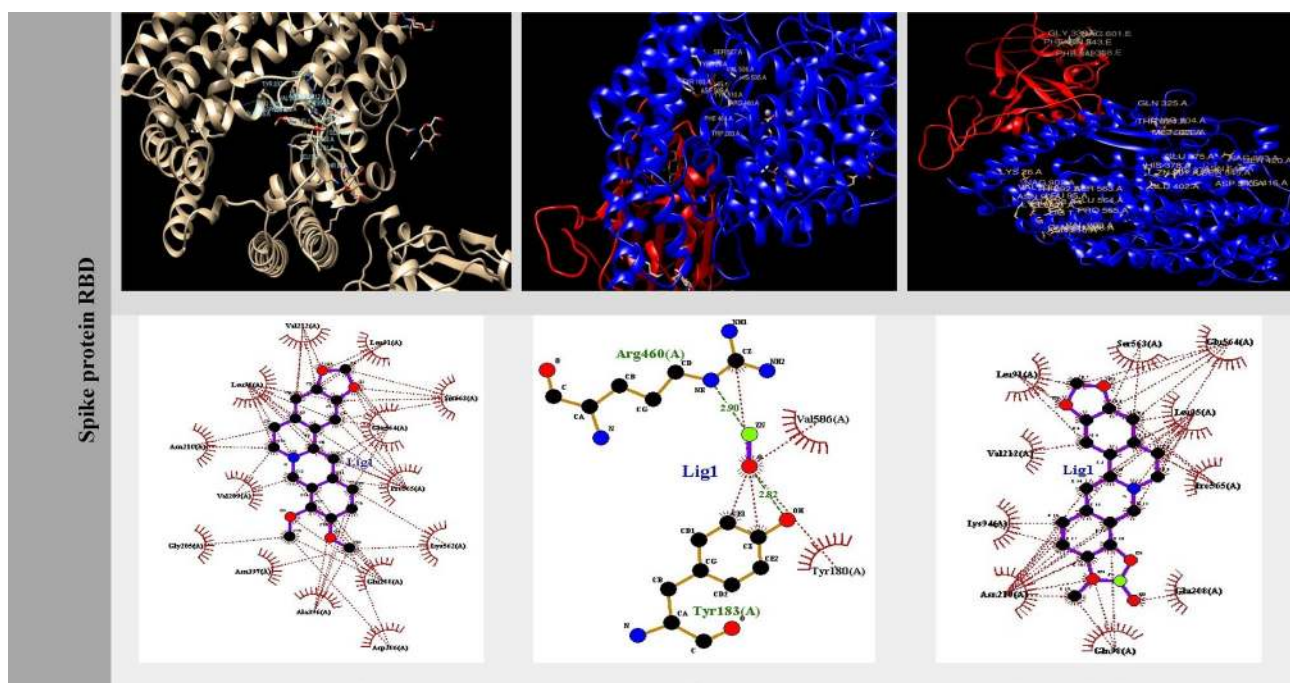


Fig. 5 (continued)

Table 4 Antiviral Activity of the tested compounds using in vitro Vero E6 toxicity and plaque reduction assay against SARS-CoV2

Tested compounds	Vero E6 IC50 ($\mu\text{g/ml}$)	Vero E6 reduction (%)	Dosage ($\mu\text{g/ml}$)	EC50 ($\mu\text{g/ml}$)	EC50/IC50%
ZnO-NPs	4.55 ± 0.03	76.00 ± 1.5	2.20 ± 0.002	1.42 ± 0.002	31.3 ± 0.7
BER	50.73 ± 0.50	80.00 ± 1.7	37.04 ± 0.300	16.70 ± 0.010	32.9 ± 0.4
ZnO/BER	1.76 ± 0.002	81.25 ± 1.2	1.64 ± 0.01	0.333 ± 0.003	18.9 ± 1.2
HCQ	1.4 ± 0.20	76.00 ± 1.8	$.10 \pm 0.050$	0.39 ± 0.009	27.5 ± 0.9

the highest protein reduction levels followed by BER and finally ZnO-NPs (Table 2). These results indicated that both of the parent compounds as well as ZnO/BER complex had an anti-COVID-19 effect through several mechanisms of action where they are involved in cell basicity that subsequently led to the inhibition of the endosomal pathway facilitated by pH-dependent cysteine protease cathepsin L (Xia et al. 2020). They prevent the virus entry by interacting with ACE2 (spike protein RBD) on the cell surface and noncompetitively inhibited spike protein. ZnO/BER complex binds by several hydrophobic interactions through Leu 91, Lys 94, Leu 95, Gln 98, Glu 208, Asn 210, Val 212, Ser 563, Glu 564 and Pro 565 that alters the ACE2 active site specificity to substrate (Bhuyan and Mugesh 2012). Furthermore, it binds to the spike protein through hydrogen bonds with Ile 666 and Pro 862 and several hydrophobic interactions with amino acids in A and B chains [Leu 864 (B), Asp 775 (B), Gly 667 (A), Pro 863 (B), Lys 733 (B), Ile 312 (A), Gln 314 (A), Thr 768 (B) and Tyr 313 (A), Pro 665(A), Leu 861(B)].

Since these hydrophobic interactions occurred in the region of the binding site, therefore they alter the protein affinity and substrate specificity (Chandel et al. 2020). These results indicated that the ZnO/BER complex is a non-competitive inhibitor that reversibly binds to the enzyme–substrate complex, yielding an inactive ESI complex (Palmer and Bonner 2007). Upon infection, the ZnO/BER complex inhibited viral replication by inhibiting PLpro activity and downregulating the expression of RdRp which consequently downregulated the viral structural protein (E-protein and spike protein).

In agreement with our results which indicates the inhibitory activity of the tested compounds towards PLpro, the previous study showed that the N-terminal of PLpro is ubiquitin like domain 2 (UL2) (amino acids 75–88) which is linked to the catalytic site. UL2 mediates a hydrophobic interaction with catalytic site, and thus any change in this region could influence substrate specificity. This inhibition might block the catalytic activity of PLpro towards ubiquitin-like interferon-stimulating 15 protein gene. Therefore,

Table 5 Antioxidant and cytotoxic effects of the tested compounds

	RBC IC ₅₀ (µg/ml)	PBMC	Antioxidants
ZnO-NPs	2140.41 ± 5.9	592 ± 11.2	2439.02 ± 12.3
BER	1349 ± 10.3	22.2 ± 0.9	121.36 ± 8.7
ZnO/BER	178.67 ± 1.1	6.2 ± 0.4	160.09 ± 2.9
HCQ	52 ± 0.9	3.2 ± 0.3	362.7 ± 6.7

antiviral interferon pathway will normally stimulated, and viral replication will be reduce in the infected cells (Shin et al. 2020).

In vitro biological activities of the ZnO/BER complex

Cytotoxicity and antioxidants properties

According to the routine drug evaluation process, drug toxicity was assessed in vitro on WBC and RBCs (Deore et al. 2019). Moreover, several studies have shown that compounds with antioxidants properties can act as anti-COVID-19 and increase drug efficacy toward the inhibition of the cytokines storm. COVID-19 was found to induce oxidative stress that led to organ failure, and consequently induced NFκβ pathway and ended by cytokines storm (Al-Taie and Victoria 2020; Soto et al. 2020). Our results in Table 5 showed that ZnO-NPs was the safest compound towards RBCs and PBMCs where it showed the highest IC₅₀ followed by BER, ZnO/BER complex and finally HCQ. In addition, the ZnO/BER complex presented the highest

Table 6 Antimicrobial activity using agar well diffusion and turbidity assays

Concentrations of the tested compounds	Agar Well Diffusion Assay				Turbidity Assay			
	Inhibition zone diameter (mm) ^a			MIC (µg/ml)	Percent of inhibition (%)			MIC (µg/ml)
	100%	50%	25%					
Gram negative Bacteria								
<i>klebsila pneumonia ATCC700603</i>								
ZnO-NPs	11 ± 0.1E ⁻⁶	ND	ND	104	65.87 ± 0.1E ⁻⁶	61.84 ± 0.1E ⁻⁶	44.13 ± 0.1E ⁻⁶	26
BER	20 ± 0.1E ⁻⁶	ND	ND	1852	61.52 ± 0.1E ⁻⁶	53.21 ± 0.1E ⁻⁶	40.38 ± 0.1E ⁻⁶	463
ZnO/BER	ND	ND	ND	ND	70.22 ± 0.1E ⁻⁶	67.83 ± 0.1E ⁻⁶	63.70 ± 0.1E ⁻⁶	41.6
Positive control	35 ± 0.1E ⁻⁶				78.91 ± 0.1E ⁻⁶			
Gram positive Bacteria								
<i>Staphylococcus aureus ATCC25923</i>								
ZnO-NPs	17 ± 0.1E ⁻⁶	ND	ND	104	87.77 ± 0.1E ⁻⁶	33.24 ± 0.1E ⁻⁶	8.09 ± 0.1E ⁻⁶	26
BER	20 ± 0.1E ⁻⁶	12 ± 0.0	ND	926	88.30 ± 0.1E ⁻⁶	67.02 ± 0.1E ⁻⁶	18.09 ± 0.1E ⁻⁶	463
ZnO/BER	15 ± 0.1E ⁻⁶	ND	ND	166.5	89.63 ± 0.1E ⁻⁶	83.24 ± 0.1E ⁻⁶	79.52 ± 0.1E ⁻⁶	41.6
Positive control	25 ± 0.1E ⁻⁶				90.43 ± 0.1E ⁻⁶			
<i>Streptococcus pyogenes EMCC1772</i>								
ZnO-NPs	12 ± 0.1E ⁻⁶	ND	ND	104	68.31 ± 0.1E ⁻⁶	50.85 ± 0.1E ⁻⁶	41.49 ± 0.1E ⁻⁶	26
BER	23 ± 0.1E ⁻⁶	15 ± 0.0	11 ± 0.1E ⁻⁶	463	64.45 ± 0.1E ⁻⁶	60.36 ± 0.1E ⁻⁶	54.97 ± 0.1E ⁻⁶	463
ZnO/BER	15 ± 0.1E ⁻⁶	ND	ND	166.5	78.69 ± 0.1E ⁻⁶	78.14 ± 0.1E ⁻⁶	77.60 ± 0.1E ⁻⁶	41.6
Positive control	35 ± 0.1E ⁻⁶				79.78 ± 0.1E ⁻⁶			
Yeast								
<i>Candida albicans EMCC105</i>								
ZnO-NPs	30 ± 0.1E ⁻⁶	25 ± 0.1E ⁻⁶	20 ± 0.1E ⁻⁶	26	25.00 ± 0.1E ⁻⁶	23.44 ± 0.1E ⁻⁶	20.31 ± 0.1E ⁻⁶	26
BER	14 ± 0.1E ⁻⁶	ND	ND	1852	35.94 ± 0.1E ⁻⁶	32.81 ± 0.1E ⁻⁶	26.56 ± 0.1E ⁻⁶	463
ZnO/BER	21 ± 0.1E ⁻⁶	14 ± 0.0	ND	83.3	40.63 ± 0.1E ⁻⁶	34.38 ± 0.1E ⁻⁶	31.25 ± 0.1E ⁻⁶	41.6
Positive control	40 ± 0.1E ⁻⁶				43.75 ± 0.1E ⁻⁶			

^aDiameter includes 5 mm well diameter

ND Not detected

MIC Minimum inhibition concentration

Table 7 Effect of BER and ZnO/BER complex alone or combined with HCQ on CBC profile and blood chemistry

	Control	BER	ZnO/BER	HCQ	HCQ + BER	HCQ + ZnO/BER
WBC ($\times 10^3/\mu\text{l}$)	6.3 \pm 3.1	9.54 \pm 3	7.8 \pm 1.2	9.2 \pm 3.4	9.85 \pm 3.5	9.2 \pm 2.6
Lymphocyte (%)	63.3 \pm 14.8	52.5 \pm 14	53 \pm 14.2	56.1 \pm 18	63.2 \pm 11	61.2 \pm 10.2
Monocytes (%)	3.9 \pm 2	4.5 \pm 0.7	4.5 \pm 0.7	3.3 \pm 0.8	3.7 \pm 0.75	3.7 \pm 0.5
Granulocyte (%)	32.8 \pm 13	43 \pm 14	42.9 \pm 0.7	40.6 \pm 17	33.1 \pm 10.8	35.1 \pm 1.2
RBC ($\times 10^5/\mu\text{l}$)	7.16 \pm 0.4	7.2 \pm 2	7.2 \pm 0.9	5.3.75 \pm 2.3	8.3 \pm 1.3	7.6 \pm 0.4
Hb (g/dl)	10.4 \pm 0.6	10 \pm 3	10.1 \pm 1.2	8.3 \pm 0.4	11.3 \pm 2.8	11.3 \pm 1.7
Hct (%)	32.3 \pm 1.2	37.23 \pm 08	31.5 \pm 2.8	27.7 \pm 10	33.9 \pm 7.9	31.2 \pm 5.3
Platelet count ($\times 10^3/\mu\text{l}$)	1116 \pm 21	1044 \pm 52	1144 \pm 25	1348 \pm 577	1158 \pm 86	1157 \pm 23
ALT (U/L)	20.4 \pm 1.2	21.5 \pm 2.1	21.9 \pm 0.01	33.44 \pm 2.3	25.6 \pm 4.5	22.6 \pm 1.2
AST (U/L)	33.8 \pm 3.4	35 \pm 1.8	33.9 \pm 1.2	102.22 \pm 21	43.2 \pm 14.8	38.7 \pm 2.8
AST/ALT	1.65	1.66	1.55	3.06	1.7	1.7
ALP (U/L)	11.8 \pm 2.5	12.9 \pm 0.96	12.1 \pm 0.25	1.64 \pm 0.6	8.5 \pm 0.4	10.2 \pm 0.9
Total protein (g%)	2.3 \pm 0.03	2.5 \pm 0.07	2.42 \pm 0.002	1.54 \pm 0.5	1.9 \pm 0.4	2.1 \pm 0.1
Albumin (g%)	0.9 \pm 0.02	1.1 \pm 0.02	0.99 \pm 0.03	0.46 \pm 0.15	0.7 \pm 0.14	0.8 \pm 0.05
D-Bilirubin (mg/dl)	0.15 \pm 0.002	0.15 \pm 0.01	0.15 \pm 0.002	0.01 \pm 0.0001	0.09 \pm 0.0004	0.15 \pm 0.02
TG (mg/dl)	155 \pm 1.5	70 \pm 6.7	100 \pm 6.9	50.44 \pm 0.9	60 \pm 0.2	60.8 \pm 2.8
Creatinine (mg/dl)	0.29 \pm 0.05	0.28 \pm 0.0004	0.28 \pm 0.008	0.24 \pm 0.01	0.26 \pm 0.01	0.29 \pm 0.02
Uric acid (mg/dl)	1.14 \pm 0.2	1.09 \pm 0.09	1.1 \pm 0.001	1.5 \pm 0.52	1.3 \pm 0.08	1.1 \pm 0.11
Urea (mg/dl)	15.5 \pm 0.3	17.5 \pm 1.7	16.5 \pm 3.1	24.28 \pm 3.5	18.3 \pm 1.08	16.9 \pm 3.6

The results are mean \pm SD

Table 8 Effect of the ZnO-NPs, BER and ZnO/BER complex on HCQ induced RBC hemolysis and WBC cytotoxicity

Compounds	RBC hemolysis		WBC cytotoxicity	
	Concentration ($\mu\text{g/ml}$)	Hemolytic (%)	Concentration ($\mu\text{g/ml}$)	Viability (%)
ZnO-NPs	68.5	0.9 \pm 0.008	12.5	53 \pm 1.3
BER	463	21.62 \pm 0.8	115.75	56 \pm 2.7
ZnO/BER	84.1	6.31 \pm 0.3	41.6	56 \pm 1.9
HCQ (+ve Control)	27.5	50.45 \pm 0.9	200	6 \pm 0.05
HCQ + ZnO-NPs	27.5 + 68.5	40.3 \pm 2.3	200 + 12.5	34 \pm 2.3
HCQ + BER	27.5 + 463	28.83 \pm 3.1	200 + 115.75	46 \pm 3.8
HCQ + ZnO/BER	27.5 + 84.1	8.11 \pm 0.7	200 + 41.6	45 \pm 0.9

The results are mean \pm SD

antioxidant capacity followed by BER, HCQ and finally ZnO-NPs.

Antibacterial effect of the ZnO/BER complex

Studies have reported that about 3.5% of COVID-19 patients are co-infected and approximately 14.3% have a secondary bacterial infection. Moreover, most critically ill patients are known to have bacterial infection which is why most COVID-19 patients received antibiotics (Chen et al. 2020a; Contou et al. 2020; Langford et al. 2020; Sharifipour et al. 2020). In our study, the ZnO-NPs, BER and ZnO/BER complex had anti-*klebsila pneumonia*, *Staphylococcus aureus*, *Streptococcus pyogenes* and *Candida albicans* with the highest antimicrobial activity showed by ZnO/BER complex followed by BER then ZnO-NPs (Table 6).

In vitro and in vivo HCQ side effects elimination

The use of HCQ is controversial (Risch 2020). It depends on pre-clinical data suggesting its anti-viral and anti-inflammatory properties. The clinical trial data demonstrated that HCQ showed no benefit for post-exposure prophylaxis. However, due to its unique pharmacokinetics, HCQ is unlikely to be beneficial in patients with COVID-19 infection. HCQ is taken for 5–10 days to achieve adequate plasma and lung concentrations (Barnabas et al. 2020). As previously mentioned, cardio-ocular toxicity is accounted in patients treated with HCQ. Therefore, the second objective in this study was to estimate the efficacy of the tested compounds against HCQ-induced toxicity in vitro and in vivo. It was found that ZnO-NPs decreased the hemolytic activity induced by HCQ by 20.11%, while the BER decreased it by 42.85% and finally the ZnO/BER complex displayed the maximum reduction value of 83.9% (Table 7). In the case of WBC, ZnO-NPs prevented HCQ cytotoxic effect towards WBC by 4.9 folds, whereas the BER and ZnO/BER complex prevented this effect by 6.7 folds approximately, as shown in Table 8.

The in vivo results indicated that the BER and ZnO/BER complex did not affect normal CBC parameters at $p < 0.05$. However, HCQ administration for 14 days significantly decreased the RBC count, Hb and Hct levels and increased platelet count. Nevertheless, co-administration of HCQ with BER or ZnO/BER complex prevented the HCQ adverse effect, as shown in Table 7. Healthy control mice that received BER or ZnO/BER complex showed lower TG levels compared to normal control mice. Furthermore, the group receiving HCQ had significantly lower serum direct bilirubin, ALP, total protein, albumin, T.G. and creatinine associated with elevated AST, ALT, AST/ALT ratio, uric acid and urea levels. Whereas, co-administration with BER moderately prevented the HCQ adverse effect. Interestingly,

our results exhibited that ZnO/BER complex co-administration with HCQ completely prevented the adverse action of HCQ on tissues (Table 7) as all parameters tested were in the normal range for control mice, at $p < 0.05$. In agreement with our results, several studies have reported that HCQ induces an increase in fibrinogen causing a decrease in plasmatic and blood viscosity (Ernst et al. 1984). A possible role in the rheological property decreases of RBCs (Bird et al. 1981). Moreover, it causes hepatic failure, toxic epidermal necrolysis and cardiotoxicity (Hashem et al. 2020). BER and ZnO-NPs act as antioxidants and have an anti-inflammatory and hepatic support action (El-Zeftawy et al. 2019; Ghaffari et al. 2019) that can eliminate the HCQ adverse effect on these vital tissues.

Conclusion

The ZnO/BER complex was successfully prepared with the freshly prepared facile mixing method of 30 ± 5 nm ZnO-NPs and BER-HCl. The adsorption of cationic BER molecules on the surface of negatively charged ZnO-NPs was confirmed by the non-covalent bond that played a major role in the reaction of ZnO-NPs with BER. ZnO/BER complex exhibits potent antioxidant, antiviral and antimicrobial activities and has been found to be effective at lower concentrations than BER or ZnO-NPs alone. The ZnO/BER complex acts as anti-COVID-19 by inhibiting the virus entry through interacting with the ACE2 enzyme on the cell surface and inhibiting the spike protein interaction. Also, the ZnO/BER complex inhibits PLpro activity and downregulates the expression of RdRp, which consequently downregulates the viral structural protein and prevents the viral replication. Finally, ZnO/BER complex eliminates the toxicity of HCQ administration. The obtained findings proved that ZnO/BER complex can offer a promising therapeutic option for managing COVID-19 infection and related bacterial co-infection that occurred in many cases. It can also be used in the therapeutic protocol using HCQ to eliminate related adverse effects and especially in case of patients suffering from autoimmune disorders and treated with HCQ.

Funding The authors did not receive any funding for this research.

Data availability The raw/processed data required to reproduce these findings cannot be shared at this time as the data also form part of an ongoing study.

Declarations

Conflict of interest All authors (D.A. Ghareeb, S.R. Saleh, M.G. Seadawy, M.S. Nofal, S.A. Abdulmalek, S.F. Hassan, S.M. Khedr, M.G. AbdElwahab, A.A. Sobhy, A.A. Abdel-Hamid, A.M. Yassin, A.A.A.

Elmoneam, A.A. Masoud, M.M.Y. Kaddah, S.A. El-Zahaby, A.M. Almahallawi, A.M. El-Gharbawy, A. Zaki, I.K. Seif, M.Y. Kenawy, M. Amin, K. Amer, M.A. El Demellawy) declare that they have no known competing financial interests or personal relationships that could appear to influence the work reported in this paper.

Ethical approval This article does not contain any studies on human participants performed by any of the authors.

Animal rights The animal experiment design protocol was approved by ethics committee of animal research in (PFIDC), SRTA-City, Institutional Animal Care and Use Committees (IACUC)/ IACUC # 19-1R-01020.

References

- Abd El-Salam M, Mekky H, El-Naggat EMB, Ghareeb D, El-Demellawy M, El-Fiky F (2015) Hepatoprotective properties and biotransformation of berberine and berberrubine by cell suspension cultures of *Dodonaea viscosa* and *Ocimum basilicum*. *S Afr J Bot* 97:191–195
- Aditya A, Chattopadhyay S, Gupta N, Alam S, Veedu AP, Pal M, Singh A, Santhiya D, Ansari KM, Ganguli M (2019) ZnO Nanoparticles Modified with an Amphipathic Peptide Show Improved Photoprotection in Skin. *ACS Appl Mater Interfaces* 11:56–72
- Agency EM (2020) COVID-19: chloroquine and hydroxychloroquine only be used in clinical trials or emergency use programmes [Online]. Available: <https://www.ema.europa.eu/en/news/covid-19-chloroquine-hydroxychloroquine-only-be-used-clinical-trials-emergency-use-programmes>. Accessed 1 Apr 2020
- Al-Taie A, Victoria A (2020) Supplementary medicines and antioxidants in viral infections: a review of proposed effects for COVID-19. *Biomed Biotechnol Res J* 4:19–24
- Barnabas RV, Brown ER, Bershteyn A, Stankiewicz Karita HC, Johnston C, Thorpe LE, Kottkamp A, Neuzil KM, Laufer MK, Deming M, Paasche-Orlow MK, Kissinger PJ, Luk A, Paolino K, Landovitz RJ, Hoffman R, Schaafsma TT, Krows ML, Thomas KK, Morrison S, Haugen HS, Kidoguchi L, Wener M, Greninger AL, Huang M-L, Jerome KR, Wald A, Celum C, Chu HY, Baeten JM (2020) Hydroxychloroquine as postexposure prophylaxis to prevent severe acute respiratory syndrome coronavirus 2 infection. *Ann Internal Med*.
- Bashmakova N, Kutovyy S, Zhurakivsky R, Hovorun D, Yashchuk V (2011) Vibrational spectra of berberine and their interpretation by means of DFT quantum-mechanical calculations. *Ukr J Phys* 56.
- Battu SK, Repka MA, Maddineni S, Chittiboyina AG, Avery MA, Majumdar S (2010) Physicochemical characterization of berberine chloride: a perspective in the development of a solution dosage form for oral delivery. *AAPS PharmSciTech* 11:1466–1475
- Belay A, Kim HK, Hwang Y-H (2017) Spectroscopic study of binding of chlorogenic acid with the surface of ZnO nanoparticles. *Russ J Phys Chem A* 91:1781–1790
- Bhogale A, Patel N, Mariam J, Dongre PM, Miotello A, Kothari DC (2013) Study of interaction of ZnO nanoparticles with human serum albumin using fluorescence spectroscopy. *AIP Conf Proc* 1512:130–131
- Bhuyan BJ, Mughesh G (2012) Antioxidant activity of peptide-based angiotensin converting enzyme inhibitors. *Org Biomol Chem* 10:2237–2247
- Biradha K (2003) Crystal engineering: from weak hydrogen bonds to co-ordination bonds. *CrystEngComm* 5:374–384

- Bird HA, Harkness J, Wright V (1981) Some rheological properties of blood during anti-rheumatoid therapy. *Pharmatherapeutica* 3:36–39
- Brand-Williams W, Cuvelier M-E, Berset C (1995) Use of a free radical method to evaluate antioxidant activity. *LWT-Food Sci Technol* 28:25–30
- Caly L, Druce JD, Catton MG, Jans DA, Wagstaff KM (2020) The FDA-approved drug ivermectin inhibits the replication of SARS-CoV-2 in vitro. *Antiviral Res* 178:104787
- Chandel V, Sharma PP, Raj S, Choudhari R, Rathi B, Kumar D (2020) Structure-based drug repurposing for targeting Nsp9 replicase and spike proteins of severe acute respiratory syndrome coronavirus 2. *J Biomol Struct Dyn*: 1–14.
- Chen X, Liao B, Cheng L, Peng X, Xu X, Li Y, Hu T, Li J, Zhou X, Ren B (2020a) The microbial coinfection in COVID-19. *Appl Microbiol Biotechnol* 104:7777–7785
- Chen Y, Liu Q, Guo D (2020b) Emerging coronaviruses: genome structure, replication, and pathogenesis. *J Med Virol* 92:418–423
- Contou D, Claudinon A, Pajot O, Micaëlo M, Longuet Flandre P, Dubert M, Cally R, Logre E, Fraissé M, Mentec H, Plantefève G (2020) Bacterial and viral co-infections in patients with severe SARS-CoV-2 pneumonia admitted to a French ICU. *Ann Intensive Care* 10:119
- Deore A, Dhumane J, Wagh R, Sonawane R (2019) The stages of drug discovery and development process. *Asian J Pharm Res Dev* 7:62–67
- Dubey A, Shetty A, Ravi G, Kiritkumar MC, Prabhu P, Hebbar S, El-Zahaby SA (2018) Development and investigation of novel solid self-nanoemulsifying system loaded with hydrochlorothiazide for the treatment of hypertension. *Int J Pharm Invest* 8:83–91
- El-Zahaby SA, Aboughaly MH, Abdelbary GA, El-Gazayerly ON (2016) Development of a novel solid self-nano-emulsifying osmotically controlled system of a centrally acting drug: preparation and in-vitro evaluation. *Inventi Impact NDDS* 2016:35–49
- El-Zeftawy M, Ghareeb D, Elbealy ER, Saad R, Mahmoud S, Elguindy N, El-Kott AF, El-Sayed M (2019) Berberine chloride ameliorated PI3K/Akt-p/SIRT-1/PTEN signaling pathway in insulin resistance syndrome induced in rats. *J Food Biochem* 43:e13049
- Ernst E, Rose M, Lee R (1984) Modification of transoperative changes in blood fluidity by hydroxychloroquine: a possible explanation for the drug's antithrombotic effect. *Pharmatherapeutica* 4:48–52
- Espitia, P., Otoni, C. & Soares, N. 2016. Zinc Oxide Nanoparticles for Food Packaging Applications.
- Estrada-Urbina J, Cruz-Alonso A, Santander-González M, Méndez-Albore A, Vázquez-Durán A (2018) Nanoscale zinc oxide particles for improving the physiological and sanitary quality of a mexican landrace of red maize. *Nanomaterials (Basel)*, 8.
- Ghaffari H, Tavakoli A, Moradi A, Tabarraei A, Bokharaei-Salim F, Zahmatkeshan M, Farahmand M, Javanmard D, Kiáni SJ, Esghaei M, Pirhajati-Mahabadi V, Monavari SH, Ataei-Pirkooch A (2019) Inhibition of H1N1 influenza virus infection by zinc oxide nanoparticles: another emerging application of nanomedicine. *J Biomed Sci* 26:70
- Ghareeb AE, Moawed FSM, Ghareeb DA, Kandil EI (2018) Potential prophylactic effect of berberine against rat colon carcinoma induce by 1,2-Dimethyl Hydrazine. *Asian Pac J Cancer Prev* 19:1685–1690
- Ghareeb DA, Abd El-Wahab AE, Sarhan EE, Abu-Serie MM, El Demellawy MA (2013) Biological assessment of *Berberis vulgaris* and its active constituent, berberine: Antibacterial, antifungal and anti-hepatitis C virus (HCV) effect. *J Med Plants Res* 7:1529–1536
- Ghareeb DA, Elwakeel EH, Khalil R, Aziz MS, El Demellawy MA (2016) Investigation of the immunomodulatory effect of *Berberis vulgaris* on core-pulsed dendritic cell vaccine. *BMC Complement Altern Med* 16:325
- Ghareeb DA, Saleh SR, Nofal MS, Kaddah MM, Hassan SF, Seif IK, El-Zahaby SA, Khedr SM, Kenawy MY, Masoud AA (2021) Potential therapeutic and pharmacological strategies for SARS-CoV2. *J Pharm Invest*, 1–16
- Hashem AM, Alghamdi BS, Algaissi AA, Alshehri FS, Bukhari A, Alfaleh MA, Memish ZA (2020) Therapeutic use of chloroquine and hydroxychloroquine in COVID-19 and other viral infections: a narrative review. *Travel Med Infect Dis* 35:101735
- Hussien HM, Abd-Elmegied A, Ghareeb DA, Hafez HS, Ahmed HEA, El-Moneam NA (2018) Neuroprotective effect of berberine against environmental heavy metals-induced neurotoxicity and Alzheimer's-like disease in rats. *Food Chem Toxicol* 111:432–444
- Irimpan L, Nampoori VPN, Radhakrishnan P, Deepthy A, Krishnan B (2007) Size dependent fluorescence spectroscopy of nanocolloids of ZnO. *J Appl Phys* 102:063524
- Jia B, Li Y, Wang D, Duan R (2014) Study on the interaction of β -cyclodextrin and berberine hydrochloride and its analytical application. *PLOS One* 9:e95498
- Jiang J, Pi J, Cai J (2018) The advancing of zinc oxide nanoparticles for biomedical applications. *Bioinorg Chem Appl* 2018:1062562
- Kadaikunnan S, Rejiniemon TS, Khaled JM, Alharbi NS, Mothana R (2015) In-vitro antibacterial, antifungal, antioxidant and functional properties of *Bacillus amyloliquefaciens*. *Ann Clin Microbiol Antimicrob* 14:9
- Kathiravan A, Paramaguru G, Renganathan R (2009) Study on the binding of colloidal zinc oxide nanoparticles with bovine serum albumin. *J Mol Struct* 934:129–137
- Kim S, Lee SY, Cho HJ (2018) Berberine and zinc oxide-based nanoparticles for the chemo-photothermal therapy of lung adenocarcinoma. *Biochem Biophys Res Commun* 501:765–770
- Langford BJ, So M, Raybardhan S, Leung V, Westwood D, Macfadden DR, Soucy JR, Daneman N (2020) Bacterial co-infection and secondary infection in patients with COVID-19: a living rapid review and meta-analysis. *Clin Microbiol Infect* 26:1622–1629
- Liu C, Zhou Q, Li Y, Garner LV, Watkins SP, Carter LJ, Smoot J, Gregg AC, Daniels AD, Jervey S, Albau D (2020a) Research and development on therapeutic agents and vaccines for COVID-19 and related human coronavirus diseases. *ACS Cent Sci* 6:315–331
- Liu J, Cao R, Xu M, Wang X, Zhang H, Hu H, Li Y, Hu Z, Zhong W, Wang M (2020b) Hydroxychloroquine, a less toxic derivative of chloroquine, is effective in inhibiting SARS-CoV-2 infection in vitro. *Cell Discov* 6:16
- Liu Q, Xie Z, Liu T, Fan J (2018) Determination of berberine hydrochloride using a fluorimetric method with silica nanoparticles as a probe. *RSC Adv* 8:6075–6082
- Mahmoud MA, Ghareeb DA, Sahyoun HA, Elshehawey AA, Elsayed MM (2016) In vivo interrelationship between insulin resistance and interferon gamma production: protective and therapeutic effect of berberine. *Evid Based Complement Alternat Med* 2016:2039897
- Minaiyan M, Ghannadi A, Mahzouni P, Jaffari-Shirazi E (2011) Comparative study of berberis vulgaris fruit extract and berberine chloride effects on acetic acid-induced colitis in rats. *Iran J Pharm Res* 10:97–104
- Nagaraju G, Udayabhanu S, Prashanth SA, Shastri M, Yathish KV, Anupama C, Rangappa D (2017) Electrochemical heavy metal detection, photocatalytic, photoluminescence, biodiesel production and antibacterial activities of Ag-ZnO nanomaterial. *Mater Res Bull* 94:54–63
- Palmer T, Bonner PL (2007) *Enzymes biochemistry, biotechnology, clinical chemistry*, Woodhead Publishing.
- Pingali S, Donahue J, Payton-Stewart F (2014) Weak C-H...X (X = O, N) hydrogen bonds in the crystal structure of dihydroberberine. *Acta crystallographica Section c Struct Chem* 70:388–391
- Raafat KM, El-Zahaby SA (2020) Niosomes of active *Fumaria officinalis* phytochemicals: antidiabetic, antineuropathic,

- anti-inflammatory, and possible mechanisms of action. *Chin Med* 15:1–22
- Repetto G, Del Peso A, Zurita JL (2008) Neutral red uptake assay for the estimation of cell viability/cytotoxicity. *Nat Protoc* 3:1125–1131
- Risch HA (2020) Early outpatient treatment of symptomatic, high-risk COVID-19 patients that should be ramped up immediately as key to the pandemic crisis. *Am J Epidemiol* 189:1218–1226
- Saleh SR, Attia R, Ghareeb DA (2018) The ameliorating effect of berberine-rich fraction against gossypol-induced testicular inflammation and oxidative stress. *Oxid Med Cell Longev* 2018:1056173
- Shang J, Wan Y, Liu C, Yount B, Gully K, Yang Y, Auerbach A, Peng G, Baric R, Li F (2020) Structure of mouse coronavirus spike protein complexed with receptor reveals mechanism for viral entry. *PLoS Pathog* 16:e1008392–e1008392
- Sharifipour E, Shams S, Esmkhani M, Khodadadi J, Fotouhi-Ardakani R, Koohpaei A, Doosti Z, Ej Golzari S (2020) Evaluation of bacterial co-infections of the respiratory tract in COVID-19 patients admitted to ICU. *BMC Infect Dis* 20:646
- Shin D, Mukherjee R, Grewe D, Bojkova D, Baek K, Bhattacharya A, Schulz L, Widera M, Mehdipour AR, Tascher G, Geurink PP, Wilhelm A, Der Heden V, Van Noort GJ, Ovaas H, Müller S, Knobloch K-P, Rajalingam K, Schulman BA, Cinatl J, Hummer G, Ciesek S, Dikic I (2020) Papain-like protease regulates SARS-CoV-2 viral spread and innate immunity. *Nature* 587:657–662
- Soto ME, Guarner-Lans V, Soria-Castro E, Manzano Pech L, Pérez-Torres I (2020) Is antioxidant therapy a useful complementary measure for covid-19 treatment? an algorithm for its application. *Medicina* 56:386
- Soudi SA, Nounou MI, Sheweita SA, Ghareeb DA, Younis LK, El-Khordagui LK (2019) Protective effect of surface-modified berberine nanoparticles against LPS-induced neurodegenerative changes: a preclinical study. *Drug Deliv Transl Res* 9:906–919
- Strekal N, Motevich I, Nowicky J, Maskevich S (2007) IR absorption and surface-enhanced Raman spectra of the isoquinoline alkaloid berberine. *J Appl Spectrosc* 74:31–37
- Taefehshokr N, Taefehshokr S, Hemmat N, Heit B (2020) Covid-19: perspectives on innate immune evasion. *Front Immunol* 11:580641–580641
- Tai W, He L, Zhang X, Pu J, Voronin D, Jiang S, Zhou Y, Du L (2020) Characterization of the receptor-binding domain (RBD) of 2019 novel coronavirus: implication for development of RBD protein as a viral attachment inhibitor and vaccine. *Cell Mol Immunol* 17:613–620
- Tang T, Bidon M, Jaimes JA, Whittaker GR, Daniel S (2020) Coronavirus membrane fusion mechanism offers a potential target for antiviral development. *Antiviral Res* 178:104792
- Wang M, Cao R, Zhang L, Yang X, Liu J, Xu M, Shi Z, Hu Z, Zhong W, Xiao G (2020) Remdesivir and chloroquine effectively inhibit the recently emerged novel coronavirus (2019-nCoV) in vitro. *Cell Res* 30:269–271
- Wen MM, Abdelwahab IA, Aly RG, El-Zahaby SA (2021) Nanophytoel against multi-drug resistant *Pseudomonas aeruginosa* burn wound infection. *Drug Delivery* 28:463–477
- Who. 2021. *Coronavirus (COVID-19) Update: FDA Authorizes Drug Combination for Treatment of COVID-19* [Online]. Available: <https://www.fda.gov/news-events/press-announcements/coronavirus-covid-19-update-fda-authorizes-drug-combination-treatment-covid-19>. Accessed 12 March 2021.
- Xia S, Liu M, Wang C, Xu W, Lan Q, Feng S, Qi F, Bao L, Du L, Liu S, Qin C, Sun F, Shi Z, Zhu Y, Jiang S, Lu L (2020) Inhibition of SARS-CoV-2 (previously 2019-nCoV) infection by a highly potent pan-coronavirus fusion inhibitor targeting its spike protein that harbors a high capacity to mediate membrane fusion. *Cell Res* 30:343–355
- Zhou Y, Hou Y, Shen J, Huang Y, Martin W, Cheng F (2020) Network-based drug repurposing for novel coronavirus 2019-nCoV/SARS-CoV-2. *Cell Discovery* 6:14
- Zou L, Dai L, Zhang X, Zhang Z, Zhang Z (2020) Hydroxychloroquine and chloroquine: a potential and controversial treatment for COVID-19. *Arch Pharmacol Res* 43:765–772

Publisher's Note Springer Nature remains neutral with regard to jurisdictional claims in published maps and institutional affiliations.

Authors and Affiliations

Doaa A. Ghareeb^{1,2,3} · Samar R. Saleh^{1,2,3} · Mohamed G. Seadawy⁴ · Mohammed S. Nofal¹ · Shaymaa A. Abdulmalek^{1,2,3} · Salma F. Hassan¹ · Shaimaa M. Khedr¹ · Miral G. Abdelwahab¹ · Ahmed A. Sobhy^{1,2,5} · Ali saber Ali Abdel-Hamid¹ · Abdelrahman Mohamed Yassin¹ · Alshimaa A. Abd Elmoneam^{2,3} · Aliaa A. Masoud^{2,3} · Mohamed M. Y. Kaddah¹ · Sally A. El-Zahaby⁶ · Abdulaziz Mohsen Al-mahallawi^{7,8} · Alaa M. El-Gharbawy¹ · Ahmed Zaki¹ · Inas k. Seif^{1,2,3} · Marwa Y. Kenawy^{2,3,9} · Magdy Amin¹⁰ · Khaled Amer¹¹ · Maha Adel El Demellawy^{1,12}

¹ Center of Excellence for Drug Preclinical Studies (CE-DPS), Pharmaceutical and Fermentation Industry Development Center, City of Scientific Research & Technological Applications, New Borg El Arab, Alexandria, Egypt

² Bio-Screening and Preclinical Trial Lab, Biochemistry Department, Faculty of Science, Alexandria University, Alexandria, Egypt

³ Biochemistry Department, Faculty of Science, Alexandria University, Alexandria, Egypt

⁴ Chemical Warfare Department, MCL Almaza, Cairo, Egypt

⁵ Clinical Pharmacy Program, Faculty of Pharmacy, Alexandria University, Alexandria, Egypt

⁶ Department of Pharmaceutics and Pharmaceutical Technology, Faculty of Pharmacy, Pharos University in Alexandria, Alexandria, Egypt

⁷ Department of Pharmaceutics and Industrial Pharmacy, Faculty of Pharmacy, Cairo University, Cairo, Egypt

⁸ School of Life and Medical Sciences, University of Hertfordshire Hosted by Global Academic Foundation, New Administrative Capital, Cairo, Egypt

⁹ Fabrication Technology Research Department, Advanced Technology and New Materials Research Institute (ATNMRI), City of Scientific Research and Technological Applications (SRTA-City), New Borg El-Arab City, Alexandria 21934, Egypt

¹⁰ Military Medical Services, Cairo, Egypt

¹¹ Egypt Center for Research and Regenerative Medicine, Cairo, Egypt

¹² Medical Biotechnology Department, Genetic Engineering and Biotechnology Research Institute, City of Scientific Research & Technological Applications, New Borg El Arab, Alexandria, Egypt